

This is an Open Access document downloaded from ORCA, Cardiff University's institutional repository: <https://orca.cardiff.ac.uk/id/eprint/101256/>

This is the author's version of a work that was submitted to / accepted for publication.

Citation for final published version:

Wagner, H. P., Kaveh, M., Gao, Q., Tan, H., Jagadish, C. and Langbein, Wolfgang 2017. Population dynamics and dephasing of excitons and electron-hole pairs in polytype wurtzite/zinc-blende InP nanowires. *Physical Review B* 95 (4) , 045305. 10.1103/PhysRevB.95.045305

Publishers page: <http://dx.doi.org/10.1103/PhysRevB.95.045305>

Please note:

Changes made as a result of publishing processes such as copy-editing, formatting and page numbers may not be reflected in this version. For the definitive version of this publication, please refer to the published source. You are advised to consult the publisher's version if you wish to cite this paper.

This version is being made available in accordance with publisher policies. See <http://orca.cf.ac.uk/policies.html> for usage policies. Copyright and moral rights for publications made available in ORCA are retained by the copyright holders.



Population Dynamics and Dephasing of Excitons and Electron-Hole Pairs in Polytype Wurtzite-Zincblende InP Nanowires

H. P. Wagner¹, M. Kaveh², Q. Gao³, H. Tan³, C. Jagadish³, and W. Langbein⁴

¹Department of Physics, University of Cincinnati, Cincinnati, OH 45221, U.S.A.

²Department of Physics and Astronomy, James Madison University, Harrisonburg, VA 22807,
U.S.A.

³Department of Electronic Materials Engineering, Research School of Physics and Engineering,
Australian National University, Canberra ACT 2601, Australia

⁴School of Physics and Astronomy, Cardiff University, Cardiff CF24 3AA, U. K.

Corresponding author: Hans-Peter Wagner

Abstract:

We investigated the dephasing and population dynamics of electron-hole (e-h) pairs and excitons in vapor-liquid-solid grown polytype wurtzite/zincblende (WZ/ZB) InP nanowires (NWs) using heterodyne four-wave-mixing (HFWM) in three-beam configuration at temperatures from 80 to 270K. The photon energy of the femtosecond excitation pulses was varied to predominantly excite either mobile excitons and e-h pairs or indirect WZ/ZB excitons. The population dynamics

reveals a multi-exponential decay with time constants ranging over six orders of magnitude. The dynamics has been interpreted by a coupled rate equation model which considers wurzite and zincblende electron states, donor electron states, and band bending trapping holes to the surface. The model reproduces the essential features of the experimentally observed dynamics at different excitation energies, fluences, and lattice temperatures. Intraband thermalization is reached within 5-50ps, after which the non-radiative recombination dominates the dynamics. Notably, the screenable surface band bending results in long lived spatially separated carriers, resulting in a photogenerated, spatially separated background electron and hole density important controlling the long-lived dynamics. .

I. INTRODUCTION

In recent years semiconductor nanowires (NWs) have attracted significant attention because of their electronic and optical properties such as their directed charge transport capabilities¹ and optical polarization sensitivities²⁻⁴. Different synthetic approaches have been developed to fabricate NWs including the vapor-liquid-solid (VLS) growth⁵⁻⁷, solution-liquid-solid (SLS) growth⁸ and template based methods⁹⁻¹¹. Due to the small radial dimensions of the NWs the design of NW heterostructures is not limited by strain as in conventional planar molecular beam epitaxy (MBE) or metal-organic-vapor-phase-epitaxy (MOVPE) thus enabling the fabrication of a wide variety of radial heterostructures as *e.g.* GaAs/AlGaAs⁷, GaAs/GaP¹² and InP/InAs¹³ core-shell NWs. Also axial NW heterostructures^{7, 14} become feasible that comprise segments of different semiconductor material with nanometer thickness along the NW¹⁵⁻¹⁷. Another interesting type of axial heterostructures uses alternating few nm short segments of the same chemical material but different crystal structure as *e.g.* in wurtzite/zincblende InP¹⁸⁻²⁰ and GaAs²¹ NWs revealing a type-II band alignment.

This flexibility in NW design and growth has enabled novel device applications including NW lasers^{10, 22, 23}, light emitting and detection devices^{2, 24-26}, ultrahigh density transistors²⁷ single-electron charging devices^{28, 29} as well as single photon emitters^{15, 30, 31} and detectors³². However, due to their large surface-to-volume ratio the electronic and optical properties of semiconductor NWs are susceptible to surface states and defects. It is therefore important to understand the processes which determine the carrier relaxation and transfer dynamics in these novel nanostructures.

Time-resolved photoluminescence (TRPL) spectroscopy using time-correlated-single-photon-counting (TCSPC) measures the dynamics of carrier transitions with a time resolution in the tens of picoseconds. TRPL measurements showed exciton recombination times faster than 80 ps⁷ for zincblende GaAs NWs and of ~1ns for GaAs/AlGaAs core-shell NWs at 20K^{7, 33, 34}, revealing the influence of carrier trapping at non-radiative surface states which is reduced by passivation of the NW surface with a material of higher band-gap. InP NWs of both zincblende (ZB)^{35, 36} and wurtzite (WZ)^{36, 37} type instead show exciton decay times in the order of 1ns even without a core-shell structure due to a three orders of magnitude slower surface recombination as compared to GaAs. Even longer exciton recombination times have been observed in axial polytype wurtzite/zincblende (WZ/ZB) GaAs NWs (3-8 ns)²¹ and in WZ/ZB InP NWs (about 8ns)¹⁸ which has been attributed to spatially indirect excitons across the WZ/ZB interfaces. Photoluminescence up-conversion experiments with a time resolution of about 200fs were used to measure the conversion times from electron-hole pairs in WZ sections to indirect WZ/ZB excitons in InP NWs under non-resonant excitation³⁸. The obtained conversion times increase with increasing NW diameter from 20 to 40ps for 50 to 160nm wide NWs.

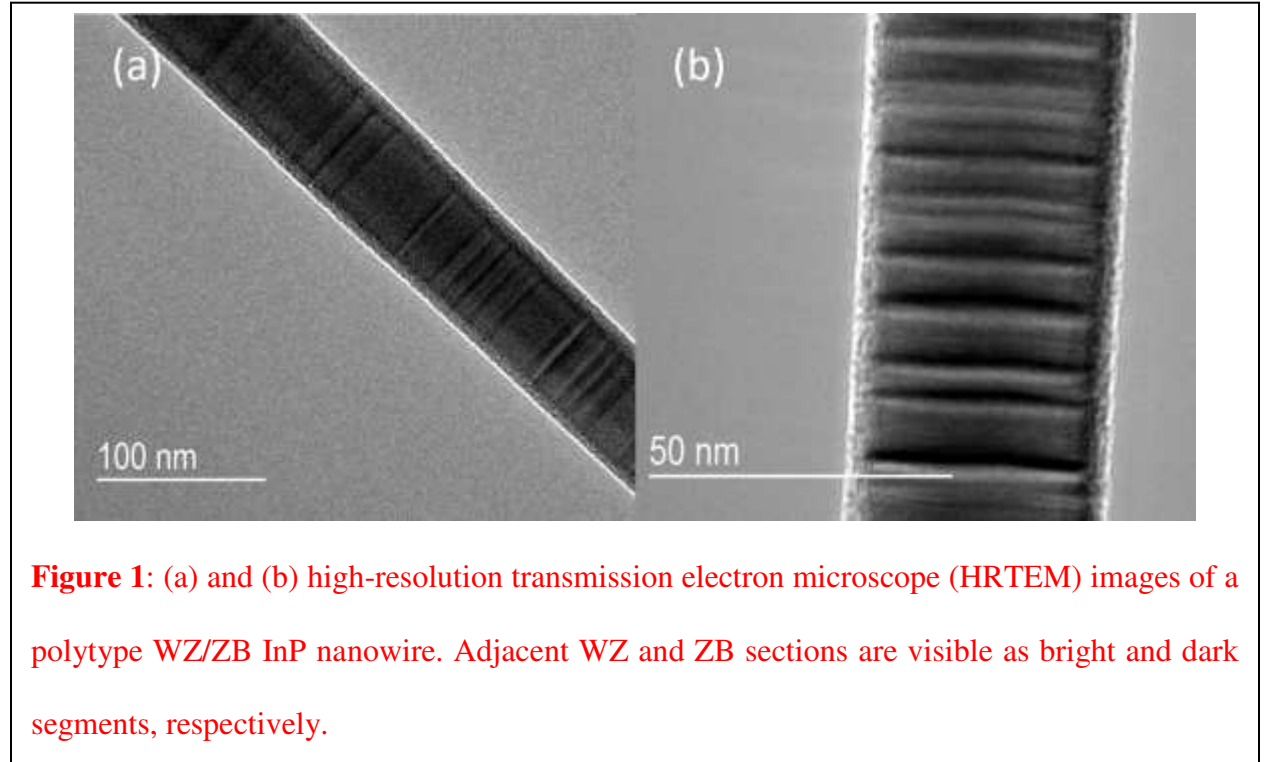
The nonlinear optical technique of four-wave mixing (FWM) is a powerful method to study coherent and incoherent carrier relaxation processes down to the femtosecond time-scale. FWM is excited by two or three mutually delayed pulses³⁹, typically with non-collinear wave vectors generating a diffracted non-linear response which can be directionally selected. While this method has been widely applied to two-dimensional (2D) and bulk semiconductors, FWM experiments on epitaxially grown or etched quantum wires (QWRs) have proven to be challenging due to a reduced signal and strong Rayleigh scattering. Only a few groups reported on directional selective FWM in t-shaped GaAs QWRs⁴⁰, in wet-chemical etched III-V⁴¹⁻⁴³ and

II-VI QWRs⁴⁴⁻⁴⁶. The more advanced technique of heterodyne FWM (HFWM)⁴⁷ combines directionally selected FWM with a highly sensitive and selective heterodyne detection⁴⁸ providing sufficient suppression of the Rayleigh scattering background.

II. EXPERIMENTAL

A. Growth of InP Nanowires

The polytype wurtzite-zincblende InP nanowires have been grown by the vapor-liquid-solid (VLS) technique⁵⁻⁷ at a growth temperature of 450°C and a V/III ratio of 300 on a fused silica substrate. As growth catalyst dispersed ~50nm diameter Au particles have been used resulting in tapered NWs with an average length of 4μm, a base diameter of 150 to 200nm and a tip diameter of ~40nm⁴⁹. The area density of the NWs on the silica substrate is ~4 NWs/μm².



High resolution transmission electron microscopy (HRTEM) micrographs reveal a high density of stacking faults resulting in WZ and ZB sections which appear as bright or dark segments,

respectively (see Figs. 1 (a) and (b)). The WZ and ZB section sizes range from few 10nm to 1nm^{18, 38, 49}. The WZ-ZB-WZ-ZB sequences define quantum wells for electrons and holes in the ZB and WZ segments, respectively, with varying confinement energies according to the length of the sections.

B. Optical Characterization of InP Nanowires

Prior to the HFWM experiments the NWs have been optically characterized by temperature- and intensity-dependent photoluminescence experiments⁴⁹ excited by a continuous-wave (cw) He-Ne laser at 1.96eV photon energy. A lens with a focal length of 125mm has been used to collimate the 2mm wide He-Ne laser beam (with Gaussian intensity profile) onto the sample resulting in an excitation area of $2 \times 10^{-5} \text{ cm}^2$. The sample was held in a closed-cycle Helium cryostat at temperatures varied between 20K and 300K. The PL from the NW ensemble was spectrally analyzed by a monochromator and detected by a photomultiplier with a GaAs cathode.

C. Heterodyne Four-Wave-Mixing Experiments

The HFWM experiments were performed using Fourier-limited pulses of about 100fs duration at 76MHz repetition rate. In these experiments the NWs were transferred onto a quartz crystal substrate and embedded into a polystyrene (PS) layer of a few ten micrometers thickness by drop casting a 5% PS in toluene solution. The NWs were randomly oriented within the PS layer and tended to accumulate in small clusters leading locally to a higher density than on the fused silica substrate. They were then covered by a second quartz substrate and mounted into a cold finger nitrogen-flow cryostat, at temperatures down to $T = 80\text{K}$. The population dynamics of excitons and $e-h$ pairs was studied by using three exciting pulses 1, 2 and 3 with different incident directions $\mathbf{k}_{1,2,3}$ and with zero delay ($\tau_{21} = 0$) between the pump pulses 1 and 2 and

variable delay time τ_{31} of the probe pulse 3. The pulses are focused onto the NW sample to a beam diameter of $26\mu\text{m}$. The spectral full-width-at-half-maximum (FWHM) of the exciting Gaussian shaped pulse intensity is about 11 nm (19 meV). The pulses were spectrally tuned from $\lambda_{\text{exc}} = 830\text{ nm}$ to 860 nm center wavelength in 10 nm steps to excite the InP NWs. Pulses 1 and 2 had equal fluences varied from 0.08 to $1.6\mu\text{J}/\text{cm}^2$ (each pulse), while the fluence of pulse 3 was kept at $0.17\mu\text{J}/\text{cm}^2$. The FWM signal was detected along the direction $\mathbf{k}_3+\mathbf{k}_2-\mathbf{k}_1$ in a square configuration in transmission geometry. To enable heterodyne detection, the pulses were frequency up-shifted with acousto-optic modulators (AOMs) by frequencies $\Omega_1/2\pi = 80\text{ MHz}$, $\Omega_2/2\pi = 79\text{ MHz}$ and $\Omega_3/2\pi = 78.8\text{ MHz}$ close to the repetition rate ($\Omega_{\text{rep}}/2\pi = 76\text{ MHz}$) of the laser. The linear pulse chirp at the sample due to the AOMs and other optics has been removed by pre-chirping in a grating based pulse compressor, as verified using a second order autocorrelation. The FWM signal in $\mathbf{k}_3+\mathbf{k}_2-\mathbf{k}_1$ direction having frequencies of $\Omega_S = \omega_0+\Omega_3+\Omega_2-\Omega_1$ plus integer multiples of Ω_{rep} is subsequently interfered in a beam splitter with a reference pulse with center frequency ω_0 and arrival time $\tau_{\text{ref}} = 0$ relative to the transmitted pulse 3. The resulting signal with frequency $(\Omega_S-\Omega_{\text{rep}})/2\pi = 1.8\text{ MHz}$ is measured by two high frequency photodiodes in balanced detection, amplified by a current preamplifier (Femto DHPA-100) and analyzed by a lock-in amplifier (SR844) using integration times of about 100 ms per point. Further details are given in the supplement of Ref. ⁽⁵⁰⁾

The same HFWM setup was applied to study the dephasing of excitons in the NW ensemble by varying the delay τ_{21} between pulses 1 and 2 (with pulse 2 being fixed in time). The reference pulse was delayed by τ_{ref} with respect to pulse 3. The measurements were performed at $\lambda_{\text{exc}} = 830\text{ nm}$ (photon energy $hc/\lambda_{\text{exc}} = 1.493\text{ eV}$) and 840 nm (1.476 eV). To measure the photon echo, the delay range τ_{ref} was scanned from -500 to 500 fs around τ_{21} with 50 fs steps. Pulse 3 was fixed

at a delay $\tau_{32} = 0.7\text{ps}$ (for $\lambda_{\text{exc}} = 830\text{nm}$) and $\tau_{32} = 1.0\text{ps}$ (for $\lambda_{\text{exc}} = 840\text{nm}$) after pulse 2. The resulting photon echo (PE) signal in direction $\mathbf{k}_3 + \mathbf{k}_2 - \mathbf{k}_1$ was measured as described earlier. The heterodyne detection scheme suppresses the Rayleigh scattering by typically 5 orders of magnitude in field, so that it is negligible compared to the shot noise.

III. RESULTS AND DISCUSSION

We commence by discussing the temperature-dependent photoluminescence measurements, revealing localized indirect e-h pairs or excitons at the WZ/ZB interfaces in polytype InP NWs. Subsequently, we investigate the population dynamics and dephasing of e-h pairs and of electrons originating from ionized donors as well as relaxation processes of differently localized e-h pairs using HFWM in three-beam geometry. For a quantitative analysis of the HFWM data we use fits with a multi-exponential function and a rate-equation model describing the population dynamics of electrons and holes.

A. Optical characterization of polytype WZ/ZB InP NWs

Figure 2 shows PL spectra obtained from a polytype InP NW ensemble with an area density of about $4\text{ NWs}/\mu\text{m}^2$ at temperatures ranging from 20K to 210K on a logarithmic scale. The sample was excited with a laser at a wavelength of 633nm with an excitation intensity of about $8\text{W}/\text{cm}^2$. The PL spectrum at 40K shows two emission bands centered at 1.48eV (837nm) and at 1.445eV (857nm). The emission band at 1.48eV is attributed to weakly localized WZ A-excitons where electrons and holes are localized in ZB and WZ segments, due to the type-II band-alignment^{18, 38, 49}. With increasing temperature above 60K, the A-exciton emission shifts to lower energy due to the temperature dependent band gap shrinkage^{49 51}. The emission band at about 1.445eV which is separated from the weakly trapped A-exciton band by about the LO-phonon energy of

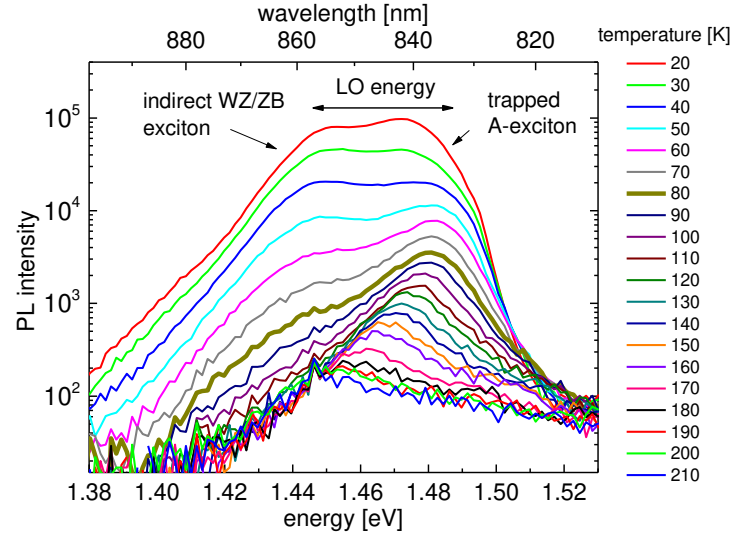


Figure 2: PL spectra at sample temperatures T ranging from 20K to 210K as labelled. The spectrum at 80K is highlighted. The excitation was at 633nm with an intensity of 8W/cm².

42.5meV^{52, 53} is attributed to an enhanced population of strongly localized indirect WZ/ZB excitons^{18, 54, 55} due to LO-phonon assisted relaxation. This interpretation is supported by determining the optical density of states (ODOS) of wurtzite A-excitons, ranging from weak to strong localization, from the PL. Assuming intraband thermal equilibrium, the ODOS is proportional to the product of the PL intensity and a Boltzmann factor $\exp(E/kT)$ as a function of emission energy E , as shown in Figure 3. The data are normalized in the flat ODOS region just above the WZ bandgap, at 1.50eV, as in this region the carriers are mobile and a thermal distribution can be expected. The increasing ODOS above 1.51eV is due to the B valence band. In this analysis we have for clarity corrected the energy for the temperature dependence of the wurtzite band gap by subtracting a Varshni expression $-\alpha T^2/(T + \beta)$ with parameters⁴⁹ $\alpha = 3.3 \times 10^{-4}$ eV/K and $\beta = 225$ K. For sample temperatures below 80K, we used a carrier temperature T somewhat higher than the lattice temperature to reproduce the optical

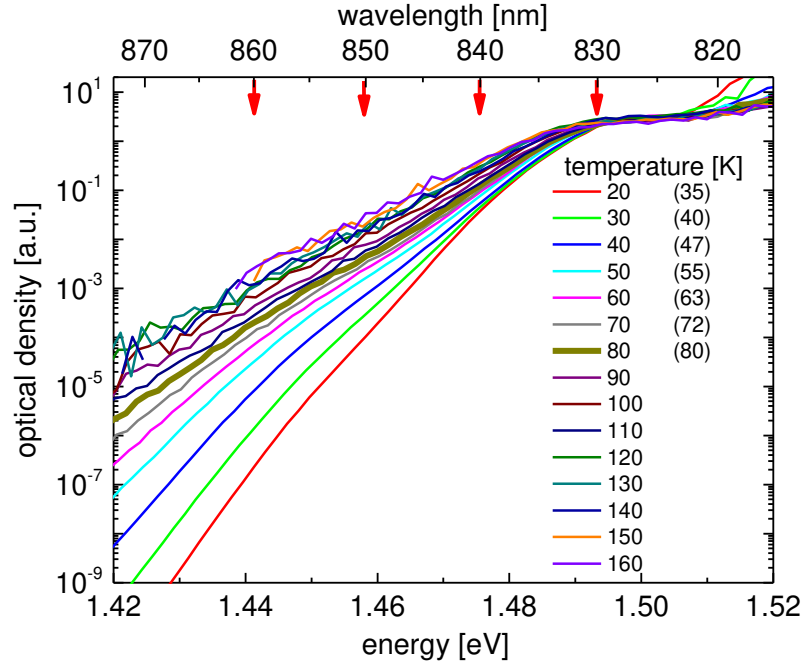


Figure 3: Optical density of states as a function of energy at temperatures ranging from 20 to 160K as labeled. The exciton density spectrum at $T = 80\text{K}$ is highlighted. The thermal band-gap shrinkage was corrected as described in the text. Carrier temperatures which deviate from the lattice temperature are shown in parentheses. The red arrows indicate the excitation center wavelengths used in the HFWM experiments.

density of states above the mobility edge. This temperature difference is due to non-complete thermalization of photoexcited carriers with the lattice during their lifetime, which is relevant at low temperatures when LO-phonons are not significantly occupied, and carrier-carrier scattering can still provide a thermalization of the mobile carriers⁵⁶. With increasing temperature the phonon-scattering rate increases, resulting in a thermal carrier distribution above 130K as seen by the essentially temperature independent retrieved ODOS. The separate emission band due to the non-thermal population accordingly vanishes above 130K (see Fig. 2). At lower temperatures instead, the steeper slopes below 1.49eV show a sub-thermal population of excitons below the

mobility edge. The spectra of the optical density show also the relative population enhancement about one LO-phonon energy below the mobility edge, which is attributed to LO-phonon assisted relaxation of electrons from the mobility edge into the indirect ZB sections. The assignment of the emission band at about 1.44eV as deeply localized WZ/ZB indirect excitons is consistent with its blue shift as a function of excitation intensity⁴⁹ attributed to state filling¹⁸ and the space-charge potential created by the indirect electron-hole density⁵⁷.

B. Population dynamics of excitons and e-h pairs in WZ/ZB InP NWs

To measure the population dynamics we used HFWM experiments with zero delay ($\tau_{21} = 0$) between “pump” pulses 1 and 2 and variable delay time τ_{31} of the “probe” pulse 3. We note that excitons in InP have a binding energy of about 5meV and are therefore mostly ionized in the investigated temperature range. We will use the term e-h pairs rather than excitons throughout when discussing the dynamics, meaning to include the bound exciton states.

1. Excitation energy dependence

The red arrows in the wavelength axis in Figure 3 indicate the excitation center wavelengths used in the HFWM experiments. The thick lines in Figs. 2 and 3 highlight the PL and optical density spectrum at 80 K at which the excitation energy dependence was measured. Figure 4 (a) shows the normalized HFWM traces for $\lambda_{\text{exc}} = 830\text{nm}$ (1.493eV), approximately $\Delta_M = 10\text{meV}$ above the exciton mobility edge for different pump-pulse fluences $\phi_{1,2}$ (where fluence $\phi_1 = \phi_2$ were varied synchronously) as labeled. The inset in Figure 4(a) shows the HFWM peak amplitude as a function of the fluence ratio $\phi_{1,2}/\phi_0$, where $\phi_0 = 1.6\mu\text{J}/\text{cm}^2$, which follows the expected linear dependence according to the signal being proportional to $E_1^* E_2 E_3$ with the fields

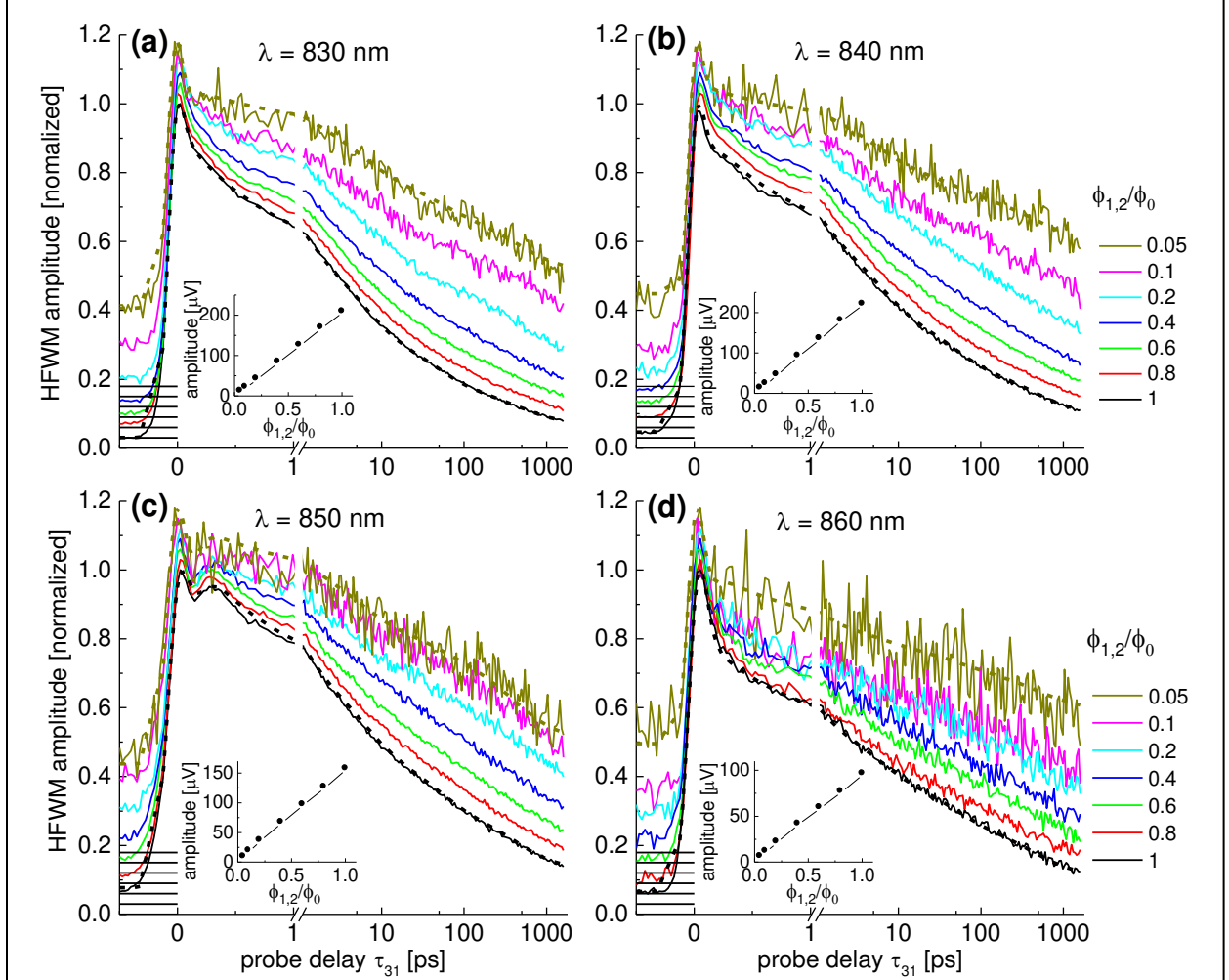


Figure 4: Normalized HFWM amplitudes at $T = 80\text{K}$ as a function of delay τ_{13} at excitation wavelengths of (a) $\lambda_{\text{exc}} = 830\text{nm}$, (b) 840nm , (c) 850nm , and (d) 860nm for different excitation fluences $\phi_{1,2}$ as labeled. The data for different fluences are vertically offset by multiples of 0.03 for clarity, see horizontal lines. The insets show the maximum HFWM amplitude versus excitation fluences $\phi_{1,2}$. Thick dashed black and dark yellow curves represent fits using the multi-exponential function given by eq. (1) as described in the text.

$E_{1,2,3}$ of the pulses. The HFWM shows an initial decay over the first picosecond, followed by a non-exponential dynamics covering time constants from 5ps to several 10ns. With increasing pump fluences we observe generally an acceleration of the decay.

Figure 4 (b) shows the normalized HFWM traces for $\lambda_{\text{exc}} = 840\text{nm}$ (1.476eV), corresponding to $\Delta_M = -7\text{meV}$ (see arrow in Fig. 3). Compared to the dynamics for $\Delta_M = 10\text{meV}$, we find a somewhat slower decay. Figure 4 (c) shows the data for $\lambda_{\text{exc}} = 850\text{nm}$ (1.458eV), corresponding to $\Delta_M = -25\text{meV}$. Here, the initial fast decay shows a minimum at about 100fs with a subsequent maximum at about 200fs. Figure 4 (d) shows the data for $\lambda_{\text{exc}} = 860\text{nm}$ (1.441eV), corresponding to $\Delta_M = -42\text{meV}$, one LO-phonon energy, below the mobility edge, resonant to deeply localized WZ/ZB indirect e-h pairs (see Figure 3). At this excitation energy we observe the longest decay times. The HFWM amplitudes as a function of ratio $\phi_{1,2}/\phi_0$ shown in the insets of Figure 4 (b) to (d) reveal similar or only slightly reduced values compared to the inset Fig. 4 (a) despite the significantly reduced excitation density at lower excitation energies. We attribute this behavior to a reduced reabsorption of the HFWM signal, as the NWs are getting transparent at energies below the WZ band gap (compare Fig. 3), showing an approximately exponential decrease of the ODOS of about one order of magnitude per 20 meV.

For a quantitative evaluation of the HFWM data we have fitted the traces with a multi-exponential function with five time constants T_i and amplitudes A_i **which is the minimum number to achieve a good agreement with the experimental data. Note that the data covers 4 orders of magnitude between time resolution and range, and the five decay times are ranging over 5 orders of magnitude. The resulting order of magnitude difference between exponential decay times allows for a well-defined multi-exponential fit.** We also included a δ -function with amplitude A_0 to model instantaneous non-resonant virtual transitions such as two-photon absorption, Kerr-effect, and relaxation processes below the temporal resolution limit. We considered that the measured HFWM data is the convolution of the multi-exponential function with a Gaussian pulse intensity autocorrelation leading to a HFWM signal of

$$F_{HFWM}(\tau_{31}) = A_0 \exp\left(-((\tau_{31} - t_0)/T_{AC})^2\right) + \sum_1^5 A_i \exp\left(-(\tau_{31} - t_0)/T_i + (T_{AC}/(2T_i))^2\right) \times \left(\frac{1}{\exp(T_{Rep}/T_i) - 1} + 1/2 \left(1 + \operatorname{erf}\left(\frac{(\tau_{31} - t_0)T_i - T_{AC}^2/2}{T_i T_{AC}} \right) \right) \right) \quad (1)$$

with T_{AC} being the pulse intensity autocorrelation time. The pulses used are well described by Gaussian function, as seen in the spectrum (see Fig. 7). The term which includes the pulse repetition period $T_{Rep} = (76 \text{ MHz})^{-1}$ considers the build up from previous pulses, and is relevant only for decay constants of the same order or longer than T_{Rep} .

After fitting all data with free time constants, we found that we could consistently describe the data using fixed time constants T_1 to T_4 of 0.7ps, 5ps, 40ps, and 400ps. The dashed curves in Fig. 4 show the corresponding fits at lowest and highest pulse fluence. The obtained amplitudes A_i are shown in Figure 5 (a-d) for the different excitation wavelengths. Due to the complexity of the carrier dynamics including different scattering processes and a set of different states with different energies and decay rates, an attribution of time constants to individual processes is bound to be approximate. Notwithstanding, we propose here an interpretation, which will be backed up in the next section by simulations.

The density of photoexcited carriers $n_{eh} = \alpha \phi_{\max} / (hc / \lambda)$ at maximum pulse fluence $\phi_{\max} = 2\phi_0$ and excitation wavelength $\lambda = 830\text{nm}$ was estimated by using the band-gap absorption coefficient of zincblende InP⁵⁸ of $\alpha = 1 \times 10^4 \text{ cm}^{-1}$ but considering the microscopic anisotropy of wurtzite InP which forbids optical transitions from the A-valence band (with symmetry Γ_9) to the conduction band (with symmetry Γ_7) for light that is polarized along the crystallographic \hat{c} -axis, along the NWs⁵⁹. This anisotropy reduces the optical absorption of the randomly oriented NWs by a factor of 2/3. Furthermore we consider the macroscopic anisotropy

which is associated with the shape of the InP NWs. The mismatch of the dielectric constants between the NW and its surrounding environment reduces the absorption coefficient by an additional factor of about 1/4⁵⁹. At highest pulse fluence ($\phi_{\text{max}} = 3.2 \mu\text{J}/\text{cm}^2$) we find a resulting e-h excitation density of about $2 \times 10^{16} \text{ cm}^{-3}$.

Due to the moderate density of photo-excited carriers, Auger recombination processes⁶⁰ are not expected to be the relevant mechanism for the observed non-exponential decay. We interpret the decay in Fig. 4 (a) and obtained amplitudes in Fig. 5 (a) as follows: The instantaneous contribution A_0 (shown at 100fs) is assigned to non-resonant virtual processes. The time constant of 0.7ps is attributed to the relaxation of highly excited e-h pairs to the mobility edge *via* carrier-carrier and LO-phonon scattering. With decreasing excitation fluence, carrier-carrier scattering is suppressed due to the reduced density of excited e-h pairs, which can be the origin of the observed reduction of amplitude A_1 . Processes relating to the time constant of 5ps are attributed to the relaxation of electrons from the mobility edge into ZB regions *via* acoustic and LO-phonon emission. This process is responsible for the observed non-thermalized PL enhancement one LO-phonon energy below the mobility edge shown in Figs. 2 and 3. The InP NWs show a background n-doping⁶¹ with a concentration of about 10^{16} cm^{-3} , resulting in a background electron density and corresponding ionized donors. Most of these electrons are expected to be trapped in the ZB sections due to the conduction band alignment. Intraband excitation of these electrons by the pump pulses leads to a modulation of the refractive index in the NWs giving rise to an additional HFWM signal.

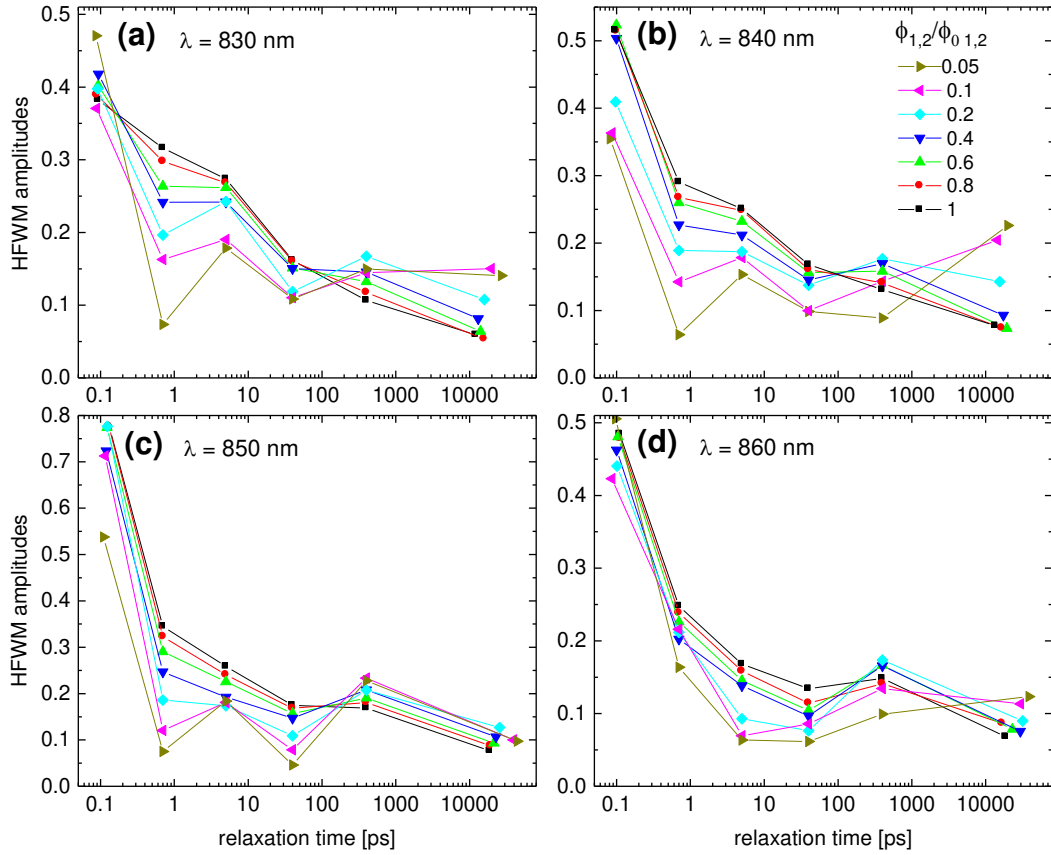


Figure 5: Amplitudes A_i of exponential decays with time constants T_i for different excitation fluences $\phi_{1,2}$ as labeled at a sample temperature of 80K, from fits of eq. (1) to the HFWM at excitation wavelengths λ_{exc} of (a) 830nm, (b) 840nm, (c) 850nm and (d) 860nm.

The intraband excited electrons which have a large excess energy relax *via* carrier-carrier scattering and LO-phonon emission towards the mobility edge on a timescale of less than 100fs, described by A_0 . Lateron, acoustic phonon assisted relaxation and thermalization will contribute to the HFWM amplitudes A_1 and A_2 . The dynamics described by the time-constant of 40ps could be due to the thermalization of electrons between the spatially separated states such as WZ / ZB, or holes between mobile and surface states. Note that at a temperature of 80K a significant

redistribution of the PL towards thermalization is observed in Fig. 3. The longer time constants T_4 of 400ps and T_5 ranging from 10ns to 30ns should be beyond thermalization and thus related to recombination. This recombination is dominantly non-radiative, as can be seen by the about 50 times reduction of the photoluminescence from 20K to 80K. Non-radiative recombination is typically explained by deep traps and described as monomolecular, especially in presence of a background doping providing a majority carrier type, electrons in the present case. The presence of a wide distribution of time constants for this process requires a spatial separation of the minority carriers, the holes, from the electrons. This can be provided by an upward band bending close to the nanowire surface due to negative surface charges ⁴⁹, which leads to a spatial separation between holes at the NW surface and electrons in the NW center, with small wavefunction overlap and consequently small recombination rates, which is consistent with the low surface recombination velocity found in InP NWs ⁶¹. The relaxation time T_5 decreases with increasing excitation fluence, which could be due to enhanced thermal activation of the surface trapped holes resulting from the screening of the band bending by the trapped hole density.

Moving the excitation pulses to smaller energies, the inter-band transitions create dominantly indirect, localized electron-hole pairs of exponentially decreasing optical density (see Fig.3), and intra-band excitation of resident electrons becomes more important in the initial dynamics in the first 10-100ps before intra-band thermalization.

For $\Delta_M = -7$ meV (Fig. 5b), the 0.7ps contribution is reduced, otherwise a similar dynamics is found. For $\Delta_M = -25$ meV (Fig. 5c), the excitation of indirect WZ/ZB e-h pairs is dominating, and the initial decay shows a minimum at approximately 100fs, which is attributed to the interband excitation of the resident electrons in the ZB trapping sites, blocking the probed transitions. Their intraband excitation results in an induced absorption, providing a HFWM

amplitude destructively interfering with the amplitude due to absorption bleaching by resonantly excited e-h pairs. At higher or lower Δ_M this effect is likely of too low strength to be visible, due to the lower occupation or the lower transition strength, respectively. In these cases, the signal resulting from the intra-band absorption is predominantly a refractive index change (phase-modulation) which is in quadrature to the absorption bleaching by resonantly excited e-h pairs consistent with the absence of the minimum. To take into account the effect of the resident electrons for $\Delta_M = -25\text{meV}$ we added an exponential function with negative amplitude A_6 into eq. (1) and fixed its relaxation time to $T_6 = 50\text{fs}$. The resulting fits for highest and lowest pump fluences are given as dashed curves in Fig. 4 (c). For $\Delta_M = -42\text{meV}$ (Fig. 5d), the excitation density of mobile e-h pairs is negligible. The observed initial dynamics is therefore created dominantly by non-resonant virtual transitions and intraband excitation of resident electrons in the ZB sections. The slower dynamics relates to the relaxation of the remaining interband excitation.

2. Temperature dependence

To study the role of phonon-assisted processes in more detail we performed additional measurements at sample temperatures of 150K, 210K and 270K. The excitation wavelength was adjusted for each temperature to compensate the temperature induced band gap shrinkage (see Fig. 2 and Ref.⁴⁹). Figure 6 (a) shows the HFWM at 150K for $\lambda_{\text{exc}} = 850\text{nm}$, $\Delta_M \sim -13\text{meV}$. A similar dynamics as for $T = 80\text{K}$, $\Delta_M \sim -20\text{meV}$ is found, including the initial minimum attributed to the intraband excitation of the trapped electrons in the ZB sections. The occurrence of the minimum despite the about 10meV higher Δ_M can be related to an increase of the

average trapped electron energy due to thermal activation. The maximum HFWM amplitude value (see inset in Figure 6 (a)) is slightly decreased compared to $T = 80\text{K}$, $\Delta_M \sim -20\text{meV}$ (see inset of Fig. 4 (c)). Fig. 6 (b) shows the amplitudes extracted from Fig. 6 (a) using eq. (1) - their general interpretation remains as described earlier.

The results for $T = 210\text{K}$ and $\lambda_{\text{exc}} = 860\text{nm}$, $\Delta_M \sim -10\text{meV}$, are given in Figure 6 (c,d). Due to the increased thermal activation of electrons from the WZ/ZB traps the induced absorption peak is not anymore noticeable. The long lifetimes T_5 are reduced, and the maximum values of the HFWM signal are about half of those at 80K , $\Delta_M \sim -7\text{meV}$. (see Fig. 4(b))

The results for $T = 270\text{K}$ and $\Delta_M \sim -10\text{meV}$ are given in Figure 6 (e,f). The amplitude A_5 with long lifetime T_5 is further reduced and the broadening of the spectral response leads to a further reduction of the maximum HFWM amplitudes.

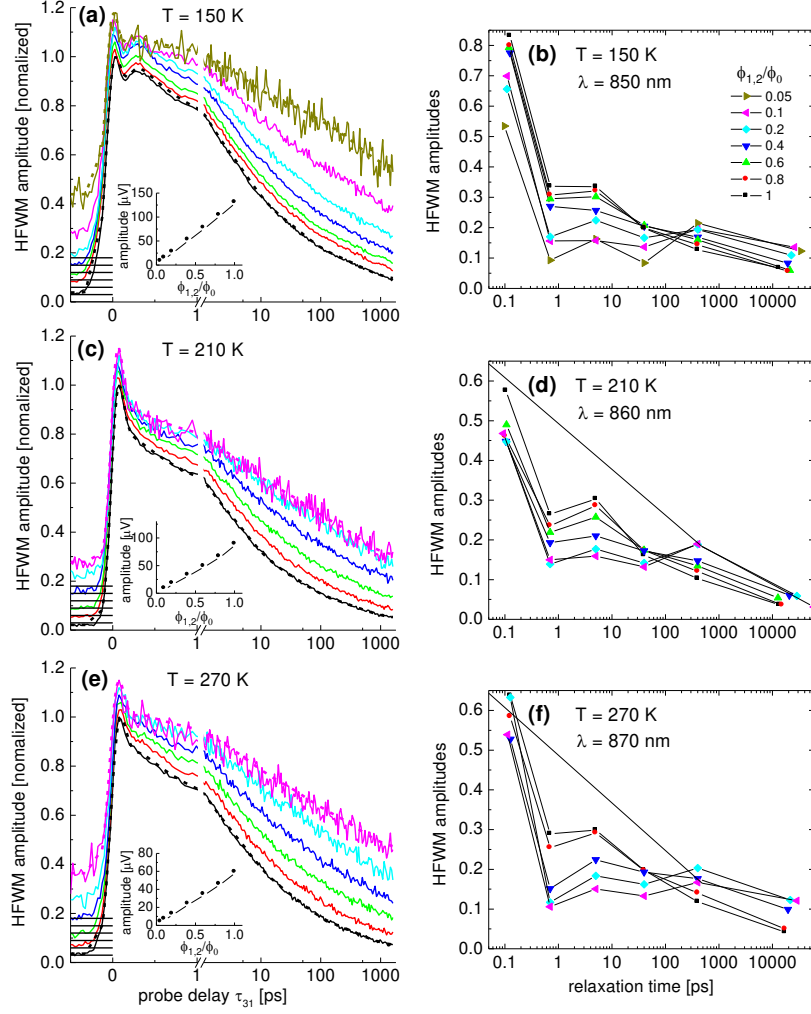


Figure 6: Left: Normalized HFWM amplitudes at (a) $T = 150$ K, (c) 210 K and (e) 270 K as a function of delay τ_{31} at excitation wavelengths of $\lambda_{\text{exc}} = 850$ nm, 860 nm and 870 nm, respectively, for different excitation fluences $\phi_{1,2}$. The data for different fluences are vertically offset by multiples of 0.03 for clarity, see horizontal lines. The insets show the maximum HFWM amplitude versus excitation fluences $\phi_{1,2}$. Thick dashed curves represent fits using the multi-exponential function given by eq. (1). Right panel: Amplitudes A_i of exponential decays with time constants T_i at sample temperatures of (b) $T = 150$ K, (d) 210 K and (f) 270 K for different excitation fluences $\phi_{1,2}$ as labeled, obtained by fitting the HFWM amplitudes with eq. (1).

C. Dephasing of excitons in WZ/ZB InP NWs

To study the dephasing of excitons in the WZ/ZB NWs photon echo (PE) experiments were performed at Δ_M of 10 meV and -7 meV. The total pump-pulse fluence $\phi = \phi_1 + \phi_2$ was set to be 0.64 and 1.6 $\mu\text{J}/\text{cm}^2$, respectively. The density of photoexcited carriers was estimated by the overlap integral of Gaussian shaped excitation pulses (with center energy E_0 and a FWHM of $\Delta E = 19\text{ meV}$) with the ODOS spectrum of InP nanowires obtained at $T = 140\text{ K}$ (from Fig. 3) where the photoexcited carriers are thermalized. The ODOS spectrum is shown as black line in Fig. 7 as a function of energy relative to exciton center energy $E_X = 1.483\text{ eV}$. The measured excitation pulse spectrum with center energy 1.476 eV (840 nm) as well as modeled Gaussian pulses at center energies 1.476 eV (840 nm) and 1.493 eV (830 nm) are given in Fig. 7 as a full grey and black dashed and dash-dotted curves, respectively. To distinguish the excitation of excitons from that of e-h pairs the optical absorption due to excitons was modeled with a broadened exciton resonance $\alpha_X(E) \propto \text{sech}^2(1.76(E - E_X)/\Delta E_X)$ with a broadening of $\Delta E_X = 21\text{ meV}$ shown as red curve in Fig. 6. The absorption of continuum states was modeled by convoluting the unit step function $\theta(E - (E_X + E_b))$ with the exciton function shifted by the exciton binding energy of

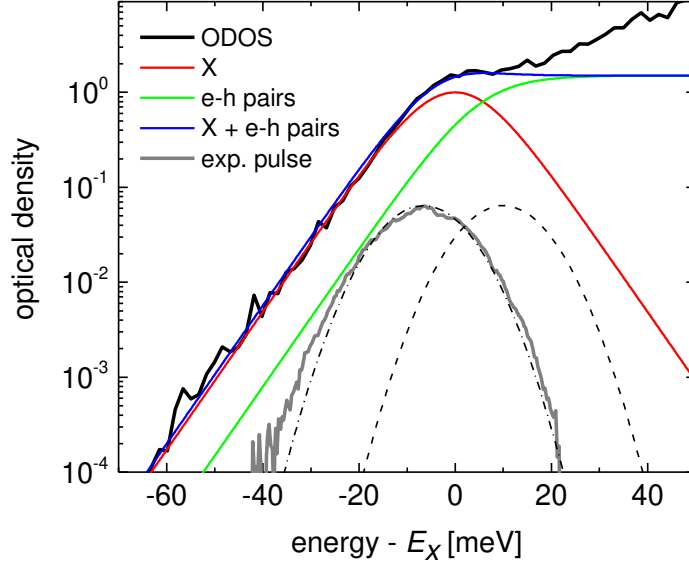


Figure 7: Optical density of states (black line) as a function of energy relative to the center energy E_X of the broadened exciton band. The red, green and blue curves are modeled exciton and continuum absorption and the resulting total absorption, respectively. Also shown is the spectrum of the excitation pulse at $\lambda_{\text{exc}} = 840\text{nm}$ (grey curve) as well as spectra of Gaussian model pulses at $\lambda_{\text{exc}} = 830\text{nm}$ and 840nm (dashed and dash-dotted curves).

$E_b = 5\text{ meV}$ resulting in a free carrier absorption $\alpha_{eh}(E) \propto 1 + \tanh(1.76(E - (E_X + E_b))/\Delta E_X)$ (green curve in Fig. 7). The total absorption spectrum of excitons and e-h pairs $\alpha(E) = c_1 \cdot \alpha_X(E) + c_2 \cdot \alpha_{eh}(E)$ was then adjusted to match the ODOS spectrum as shown as a blue curve in Fig. 7. The remaining deviation at higher energies is due to the onset of the absorption due to the B-valence band and is not relevant for the excitation spectra used.

At excitation pulses at $\lambda_{\text{exc}} = 830\text{nm}$ we find a ratio of the pulse overlap integral with excitons O_X and e-h pairs O_{eh} to be $O_X/O_{eh} = 0.54$, so that 35% of the generated pairs are

excitons. Using the previous estimate relating a pulse fluence of $3.2 \mu\text{J}/\text{cm}^2$ to a pair density of $2 \times 10^{16} \text{ cm}^{-3}$ (see section B.1.), a pulse fluence of $0.64 \mu\text{J}/\text{cm}^2$ is then estimated to result in an exciton and e-h pair density of about $1.4 \times 10^{15} \text{ cm}^{-3}$ and $2.6 \times 10^{15} \text{ cm}^{-3}$, respectively. For $\lambda_{\text{exc}} = 840\text{nm}$ we find an overlap integral ratio of $O_X/O_{eh} = 2.26$, thus about 70% of photo excited pairs are excitons. Using the relative change of O_X and O_{eh} compared to $\lambda_{\text{exc}} = 830\text{nm}$, we find the density of excitons of $4.3 \times 10^{15} \text{ cm}^{-3}$ and e-h pairs of $1.3 \times 10^{15} \text{ cm}^{-3}$, at a pulse fluence of $1.6 \mu\text{J}/\text{cm}^2$. Using these densities, we estimated the expected exciton dephasing time T_{coh} using the relationship

$$\frac{1}{T_{\text{coh}}} = \gamma_{bg} + \gamma_{ac}T + \gamma_{LO} \frac{1}{\exp(E_{LO}/(kT)) - 1} + \gamma_{XX}N_X + \gamma_{Xeh}N_{eh} \quad (2)$$

In eq. (2) the dephasing rate γ_{bg} accounts for the background dephasing due to scattering of excitons with impurities and defects, and radiative decay, γ_{ac} is the acoustic phonon scattering parameter, γ_{LO} is the LO-phonon scattering parameter, the factor $(\exp(E_{LO}/(kT)) - 1)^{-1}$ describes the thermal LO-phonon population with k being the Boltzmann constant and E_{LO} being the LO-phonon energy. γ_{XX} is the exciton-exciton scattering parameter with N_X being the generated exciton density and γ_{Xeh} is the exciton-*eh*-pair scattering parameter with generated e-h pair density N_{eh} . Using parameters $\gamma_{bg} = 0.11 \text{ ps}^{-1}$, $\gamma_{ac} = 0.007 \text{ ps}^{-1} \text{ K}^{-1}$ and $\gamma_{LO} = 21 \text{ ps}^{-1}$ from measurements on GaAs quantum wells ⁶² and $\gamma_{XX} = 1.6 \times 10^{-4} \text{ cm}^3 \text{ s}^{-1}$ and $\gamma_{Xeh} = 1.6 \times 10^{-3} \text{ cm}^3 \text{ s}^{-1}$ on undoped bulk GaAs ⁶³ we expect dephasing times of $T_{\text{coh}} = 330\text{fs}$ and 450fs for $\lambda_{\text{exc}} = 830\text{nm}$ and 840nm at the applied pump fluences.

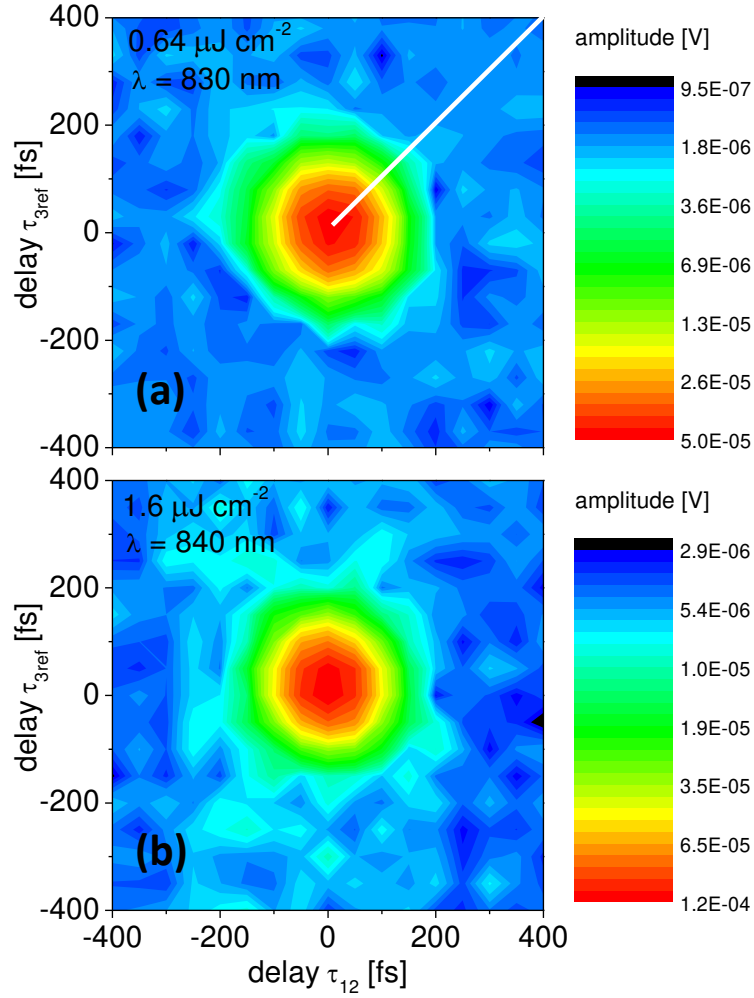


Figure 8: Two-dimensional contour plot of HFWM amplitudes obtained from of the PE experiment. (a)excitation wavelength of $\lambda_{exc} = 830\text{nm}$, pump pulse fluence $1.6\mu\text{J}/\text{cm}^2$ and (b) of $\lambda_{exc} = 840\text{nm}$, $0.64\mu\text{J}/\text{cm}^2$, on logarithmic color scales as given. The white line in the upper quadrant in Fig. 8 (a) indicates where a PE signal would be expected.

Figures 8 (a) and (b) show two-dimensional contour plots of the HFWM amplitude obtained from photon echo (PE) experiments as a function of time delay τ_{12} between pump pulses 1 and 2 and of delay τ_{3ref} of the reference pulse with respect to pulse 3. The delay of pulse 3 to pulse 2

was $\tau_{23} = 0.7$ ps for $\lambda_{\text{exc}} = 830$ nm and at $\tau_{23} = 1.0$ ps for $\lambda_{\text{exc}} = 840$ nm to suppress non-resonant responses. For dephasing times comparable or longer than the pulse duration (100 fs) a PE signal is expected in the upper quadrant as indicated by the white line in Fig. 8 (a). The virtually symmetric data at both excitation wavelengths shows that the dephasing time is significantly below 100 fs, inconsistent with the above estimated T_{coh} . We attribute the observed faster dephasing to the scattering of excitons with the electron background density resulting from a donor concentration in the order of $1 \times 10^{16} \text{ cm}^{-3}$ ⁶¹. Using γ_{Xeh} as given above, the background density results in a dephasing time of 60 fs by exciton–electron scattering, consistent with the measurements. Note that the broadening of about 21 meV in the absorption model corresponds to a dephasing time of about 60 fs ($\text{FWHM} = \hbar/T_2$), consistent with the above estimate. The presence of background electrons is also affecting the population dynamics as discussed earlier.

D. Modelling of the population dynamics

Fitting the population dynamics with eq. (1), i.e. a sum of exponential decays, is a general way to extract the dominating time constants of the dynamics and their weight. However, it assumes exponential decays, which might not be capturing the specific physical process underlying the dynamics. For our data, taken at temperatures of 80 K or higher, we note that recombination processes are dominated by electron-hole pairs due to thermal ionization of excitons, and the resulting recombination is bimolecular. To interpret the data in terms of the carrier dynamics, we have therefore developed a model including the essential ingredients of the system, which are sketched in Fig. 9¹⁸ in terms of excitation (a) and relaxation (b) pathways, considering WZ and ZB sections, donors, and surface traps for holes. The pathways are captured in a coupled rate equation model. The model includes (i) optical excitation of electron-hole pairs

(ii) optical interband excitation, (iii) intraband relaxation and activation respecting detailed balance, and (iv) bimolecular radiative and (v) [monomolecular non-radiative hole recombination](#).

The coupled rate equations are given by:

$$\begin{aligned}
\frac{dn_f}{dt} &= +P(t)(n_{\text{exc},f} + (n_D + n_T + n_m)\zeta_{\text{intra,cb}}) - \gamma_{fm}n_f \\
\frac{dn_m}{dt} &= +\gamma_{fm}n_f + \gamma_{Dm}n_D + \gamma_{Tm}n_T + P(t)(n_{\text{exc},m} - n_m\zeta_{\text{intra,cb}}) - (\tilde{\gamma}_{mD} + \gamma_{mT} + \tilde{\gamma}_m p_m)n_m - \gamma_{nr}p_m - \tilde{\gamma}_m p_S n_m \\
\frac{dn_D}{dt} &= +\tilde{\gamma}_{mD}n_m + P(t)(\tilde{n}_{\text{exc},D} - n_D\zeta_{\text{intra,cb}}) - (\gamma_D p_m + \gamma_{Dm})n_D \\
\frac{dn_T}{dt} &= +\gamma_{mT}n_m + P(t)(n_{\text{exc},T} - n_T\zeta_{\text{intra,cb}}) - (\tilde{\gamma}_T p_m + \gamma_{Tm})n_T \\
\frac{dp_S}{dt} &= +\tilde{\gamma}_{pS}p_m - \tilde{\gamma}_{Sp}p_S - \tilde{\gamma}_m p_S n_m \\
\frac{dp_m}{dt} &= +\gamma_{fm}p_f + \tilde{\gamma}_{Sp}p_S + P(t)(n_{\text{exc},m} + \tilde{n}_{\text{exc},D} + n_{\text{exc},T} - p_m\zeta_{\text{intra,vb}}) - (\gamma_D n_D + \tilde{\gamma}_T n_T + \tilde{\gamma}_m n_m + \tilde{\gamma}_{pS} + \gamma_{nr})p_m \\
\frac{dp_f}{dt} &= +P(t)(n_{\text{exc},f} + p_m\zeta_{\text{intra,vb}}) - \gamma_{fm}p_f
\end{aligned}
\tag{3}$$

The densities of electrons are separated into n_f , highly excited in the conduction band, n_m , at the WZ band edge, n_D , bound to donors, and n_T , trapped in ZB sections. The densities of holes are separated into p_f , highly excited in the valence band, and p_m at the WZ valence band edge and p_S trapped at the NW surface (see Fig. 9 (b) on the left) due to band bending. We consider

excitation pulses of power $P(t) = \frac{F}{\sigma\sqrt{2\pi}} \exp(-t^2/2\sigma^2)$ with a Gaussian broadening of full width at half maximum of $\sqrt{8\ln 2}\sigma = 100$ fs and the pulse fluence F . In the simulation we use a unitless F , moving the units into the coefficients, with $F = 1$ referring to the highest used pump-pulse fluence $2\phi_0 = 3.2\mu\text{Jcm}^{-2}$. The excitation density $n_{\text{exc},f}$ is describing the interband

absorption at the excitation photon energy. n_f is furthermore populated by intraband absorption

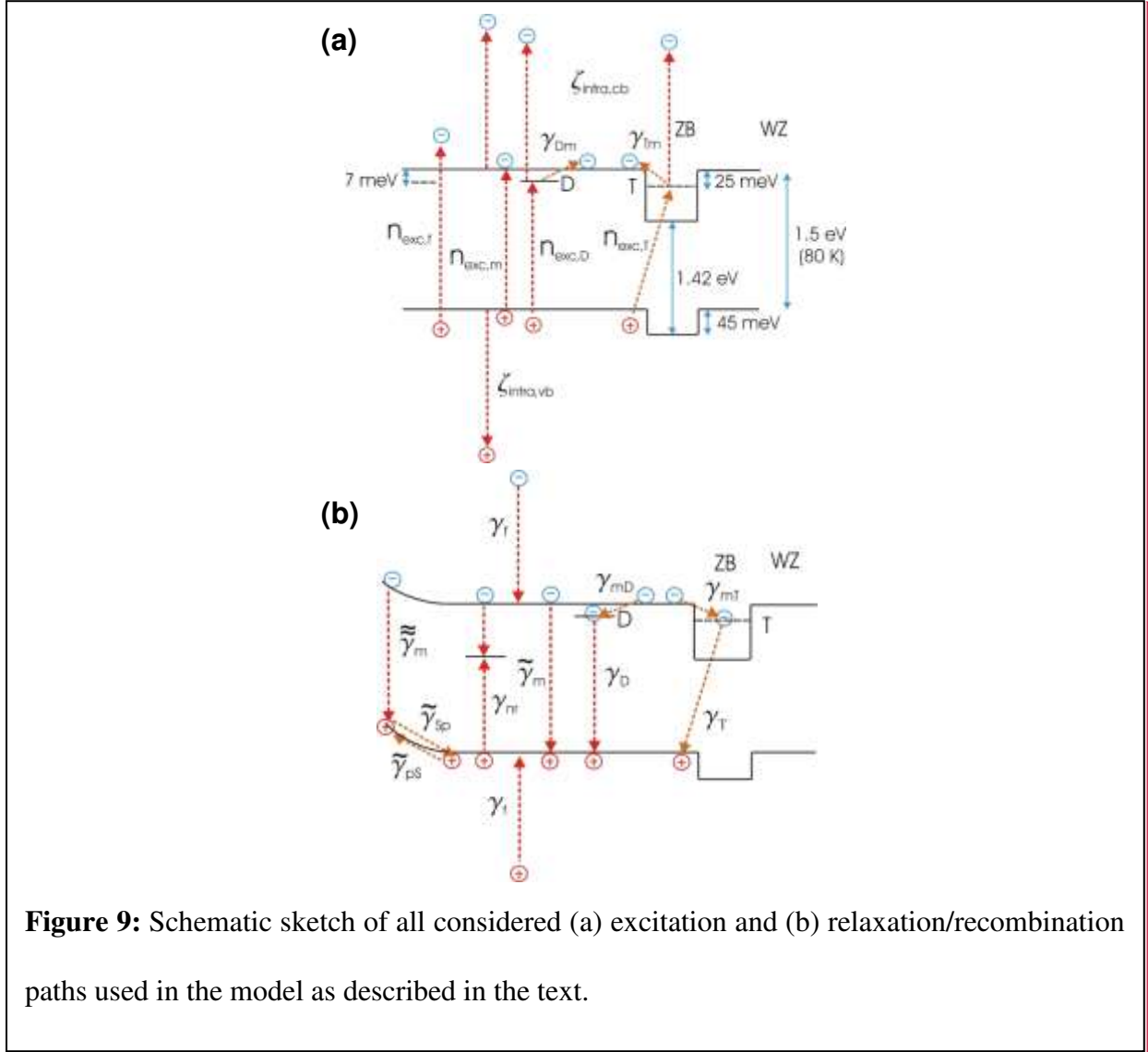


Figure 9: Schematic sketch of all considered (a) excitation and (b) relaxation/recombination paths used in the model as described in the text.

[WL2]from n_m , n_D and n_T , with a transition probability $\zeta_{\text{intra,cb}}$ for $F = 1$, and in the same way populated from p_m and p_S with the probability $\zeta_{\text{intra,vb}}$ for $F = 1$, as indicated in Fig. 9 (a). The electrons n_f and holes p_f relax with the rate γ_{fm} to the mobility edge as indicated in Fig. 9 (b). Electrons n_m and holes p_m at the mobility edge are generated in pairs by optical excitation with the density $n_{\text{exc,m}}$. Holes p_m are also generated by optical excitation into donors n_D and

trapped states n_T in the ZB sections with excitation densities $\tilde{n}_{exc,D} = n_{exc,D}(1 - n_D / n_{D_0})$ and $n_{exc,T}$, respectively. Donor state saturation was taken into account by the factor $(1 - n_D / n_{D_0})$ with n_{D_0} being the donor density in the nanowires. Holes are captured at the NW surface (p_S) via diffusion and subsequent acoustic or LO-phonon emission with rate $\tilde{\gamma}_{pS} = \gamma_{pS}(1 - p_S / p_{S_0})$. The saturation of surface charges by holes was taken into account by the factor $(1 - p_S / p_{S_0})$ with p_{S_0} being the saturation density of captured holes. The relaxation of electrons n_m into n_D or n_T via acoustic or LO-phonon emission and carrier-carrier scattering is considered by the rates $\gamma_{mD} = \gamma_{mT} = \gamma_{ph}(1 + (n_m + p_m) / n_{sc})$, where n_{sc} is the density at which carrier-carrier and phonon-assisted scattering are comparable. Corresponding thermal activation processes respecting detailed balance are added, with rates $\gamma_{Dm} = (T / T_0)^{3/2} \tilde{\gamma}_{ph} \exp(-\Delta_D / kT)$, and $\gamma_{Tm} = 2\gamma_{ph} \exp(-\Delta_T / kT)$ respectively, where Δ_D and Δ_T denote the donor binding energy and average localization energy of electrons in ZB sections, respectively. The factor $(T / T_0)^{3/2} \tilde{\gamma}_{ph}$ in rate γ_{Dm} with $T_0 = 80K$ and $\tilde{\gamma}_{ph} = 8.5\gamma_{ph}$ models the effective density of states in the conduction band as a function of temperature (the density of donor states is independent of temperature) and the prefactor 8.5 is adjusted to provide detailed balance between electrons n_m in the conduction band with the effective mass of ¹⁸ $0.073 m_e$ and neutral donors n_D at a background donor concentration of $1 \times 10^{16} \text{ cm}^{-3}$. The factor 2 in the rate γ_{Tm} models the volume ratio of WZ to ZB sections which is approximately 1:2. Trapped holes p_S are thermally activated to the valence band with a rate $\tilde{\gamma}_{Sp} = 5\gamma_{pS} \exp(-\Delta_S(1 - p_S / p_{S_0}) / kT)$ where the factor

5 takes into account a surface band bending which affects ~20% of the total NW volume. Δ_S is the trapping energy of holes at the surface. The density dependence of the trapping energy $\Delta_S(1-p_S/p_{S_0})$ is modeling the screening of the surface band bending with a saturation density of p_{S_0} . The saturation of n_T has been neglected, motivated by the expected high density of states in the ZB sections of the nanowires compared to the excitation densities used. We consider the bimolecular radiative recombination of n_m , n_T , and n_D with p_m using the rates $\tilde{\gamma}_m = \gamma_m(T/T_0)^{-3/2}$, $\tilde{\gamma}_T = \gamma_T(T/T_0)^{-3/2}$ and γ_D , respectively. The factor $(T/T_0)^{-3/2}$ in the rate $\tilde{\gamma}_m$ (with $T_0 = 80\text{K}$) models the band-band radiative lifetime considering momentum conservation during radiative recombination of electrons and holes⁶⁴. A bimolecular radiative recombination of n_m with surface holes p_S is taken into account using rate $\tilde{\gamma}_m = \gamma_m(T/T_0)^{-3/2} \exp(-\Delta_S(1-p_S/p_{S_0})/kT)$ differing from the bulk rate by the reduced thermal occupation of electrons at the surface due to the band bending. The non-radiative decay between mobile electrons n_m and holes p_m due to volume defects has been considered by rate γ_{nr} . It is assumed to be monomolecular in the holes considering that due to the high n-doping, the hole trapping by the defects is expected to be the rate limiting process (see Fig. 9(b)). Since the excitation energies in the experiments are smaller than the band gap of the ZB sections, the direct excitation of e-h pairs in the ZB sections was neglected.

Any deviation of densities $n_f(t), n_m(t), n_D(t), n_T(t), p_S(t), p_m(t), p_f(t)$ from quasi-equilibrium values $\bar{n}_f, \bar{n}_m, \bar{n}_D, \bar{n}_T, \bar{p}_S, \bar{p}_m, \bar{p}_f$ (with $\bar{n}_f = \bar{p}_m = \bar{p}_f \approx 0$) causes a change of the susceptibility $\chi = \chi_R + i\chi_I$ where the real part accounts for changes of the phase of the transmitted field, while the imaginary part changes the amplitude. The quasi-equilibrium values

depend on the lattice temperature and on the repetition frequency of the exciting laser pulses and were therefore determined considering the repetition rate of 76 MHz used in the experiments.

The resulting HFWM amplitude is given by

$$E_{FWM} = B | C_{fe} n_f(t) + C_{me} (n_m(t) - \bar{n}_m) + C_D (n_D(t) - \bar{n}_D) + C_T (n_T(t) - \bar{n}_T) + C_S p_S(t) + C_{mh} (p_m(t) - \bar{p}_m) + C_{fh} p_f(t) |$$

(4)

with complex constants $C_{fe}, C_{me}, C_D, C_T, C_P, C_{mh}, C_{fh}$ which account for the relative contribution of the various electron and hole dynamics types. For simplicity we assume that (besides C_T) all constants are solely imaginary and caused by Pauli-blocking, while C_T represents changes of the refraction index and thus is real. The factor B determines the overall magnitude of the calculated amplitude trace with the experimental data.

For the calculations the relaxation rates $\gamma_f = 20\text{ps}^{-1}$, $\gamma_{ph} = 0.14\text{ps}^{-1}$ as well as the bimolecular recombination rates $\gamma_m = 1.25 \times 10^{-8}\text{s}^{-1}\text{cm}^3$, $\gamma_D = 2.5 \times 10^{-8}\text{s}^{-1}\text{cm}^3$ and $\gamma_T = 5 \times 10^{-10}\text{s}^{-1}\text{cm}^3$ have been kept constant for all excitation wavelengths and pulse fluences. The bimolecular rate $\tilde{\gamma}_m$ corresponds to an exponential decay time of 1ns at 20K at a hole concentration of $1 \times 10^{16}\text{cm}^{-3}$ compatible with earlier time-resolved measurements at low temperature^{36, 37, 49}. The rate γ_T corresponds to an exponential decay time of 200ns at a hole

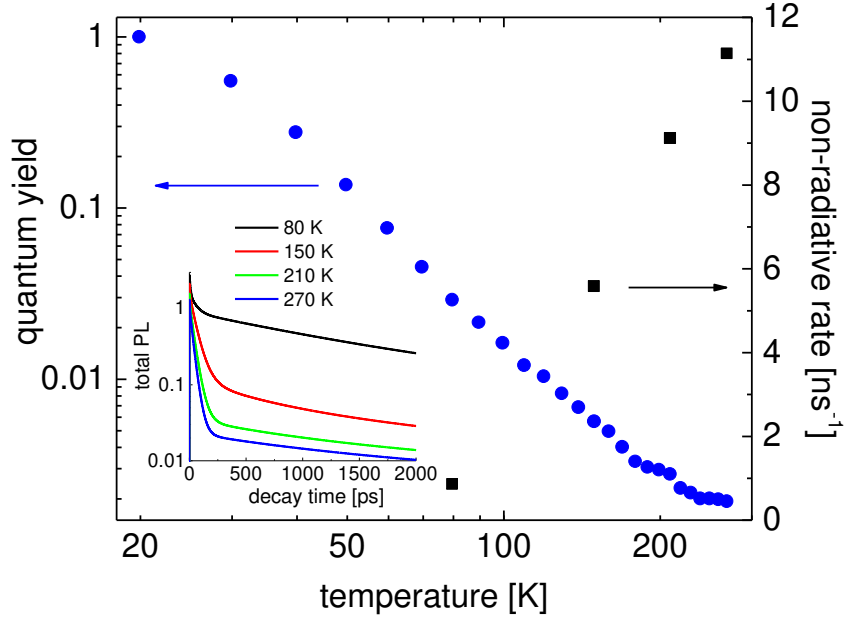


Figure 10: Quantum yield as a function of temperature (full blue circles) obtained from the normalized spectrally integrated PL intensity from Fig. 2. The squares show the derived rates γ_{nr} for temperatures 80, 150, 210 and 270K using eq. (3). The inset shows the total photon emission rate for temperatures as labeled, as function of time after excitation.

[WL4] concentration of $1 \times 10^{16} \text{ cm}^{-3}$ which is compatible with recent time-resolved measurements revealing lifetimes up to 100ns at 20K⁴⁹ and with the long decay time T_5 obtained in section III.B.1. For rates γ_{Dm} and γ_{Tm} the binding energy of $\Delta_D = 7 \text{ meV}$ ⁶⁵ and an average trapping energy $\Delta_T = 25 \text{ meV}$ consistent with the observation of induced absorption (see Fig. 3 (c)) were chosen. The total donor concentration was set to $n_{D_0} = 1 \times 10^{16} \text{ cm}^{-3}$. The saturation density of trapped surface holes was assumed to be $p_{S_0} = 4 \times 10^{15} \text{ cm}^{-3}$. Intraband transition probabilities $\zeta_{\text{intra,cb}}$ and $\zeta_{\text{intra,cb}}$ were taken to be 0.05 for all excitation wavelengths. For the rate γ_{Sp} a trapping energy of $\Delta_S = 200 \text{ meV}$ was used, providing surface trapping even at 270K which is

important obtain the observed long lifetimes T_5 at high temperatures. The non-radiative rate γ_{nr} due to volume defects was determined matching the time-integrated photon $|\lambda_{WLS}|$ emission $\int (\gamma_D n_D + \tilde{\gamma}_T n_T + \tilde{\gamma}_m n_m + \tilde{\gamma}_m n_m) p_m + \tilde{\gamma}_m n_m p_S dt$, calculated with eq. (3), to the measured temperature dependence of the spectrally integrated PL intensity evaluated from Fig. 2. A quantum yield of near unity was assumed for the PL at 20K. The experimentally observed temperature dependence of the quantum yield is shown as blue full circles in Fig. 10. The red squares in Fig. 10 show the derived rates γ_{nr} for temperatures 80, 150, 210 and 270K. The calculated total photon emission rate $(\gamma_D n_D + \tilde{\gamma}_T n_T + \tilde{\gamma}_m n_m + \tilde{\gamma}_m n_m) p_m + \tilde{\gamma}_m n_m p_S$ at low incident pump fluence ($F = 0.1$) is given in the inset of Fig.10 at temperatures as labeled, as function of time after excitation.

Table 1: Values of all parameters used to calculate the HFWM decay curves with eq. (3) and (4) at different excitation wavelengths, excitation fluences and temperatures as described in the text.

Wavelength:	830 nm	840 nm	850 nm	860 nm	850 nm	860 nm	870 nm
Temperature:	80 K	80 K	80 K	80 K	150 K	210 K	270 K
$n_{exc,f} [\text{cm}^{-3}]$	0.4×10^{16}	0.1×10^{16}	0	0	0	0.1×10^{16}	0.1×10^{16}
$n_{exc,m} [\text{cm}^{-3}]$	1.6×10^{16}	1.1×10^{16}	0.2×10^{16}	0	0.7×10^{16}	1.1×10^{16}	1.1×10^{16}
$n_{exc,D} [\text{cm}^{-3}]$	0.4×10^{16}	0.37×10^{16}	0.08×10^{16}	0	0.26×10^{16}	0.37×10^{16}	0.37×10^{16}
$n_{exc,T} [\text{cm}^{-3}]$	0.15×10^{16}	0.15×10^{16}	0.15×10^{16}	0.06×10^{16}	0.15×10^{16}	0.15×10^{16}	0.15×10^{16}
$\zeta_{\text{intra,vb}}$	0.05	0.05	0.05	0.05	0.05	0.05	0.05
$\zeta_{\text{intra,cb}}$	0.05	0.05	0.05	0.05	0.05	0.05	0.05
$\gamma_{fm} [\text{ps}^{-1}]$	20	20	20	20	20	20	20
$\gamma_{ph} [\text{ps}^{-1}]$	0.14	0.14	0.14	0.14	0.14	0.14	0.14

γ_{pS} [ps ⁻¹]	0.02	0.02	0.02	0.02	0.02	0.02	0.02
γ_{nr} [ns ⁻¹]	0.83	0.83	0.83	0.83	5.9	11.1	16.7
γ_m [s ⁻¹ cm ³]	1.25x10 ⁻⁸	1.25x10 ⁻⁸	1.25x10 ⁻⁸	1.25x10 ⁻⁸	1.25x10 ⁻⁸	1.25x10 ⁻⁸	1.25x10 ⁻⁸
γ_D [s ⁻¹ cm ³]	2.5x10 ⁻⁸	2.5x10 ⁻⁸	2.5x10 ⁻⁸	2.5x10 ⁻⁸	2.5x10 ⁻⁸	2.5x10 ⁻⁸	2.5x10 ⁻⁸
γ_T [s ⁻¹ cm ³]	5x10 ⁻¹⁰	5x10 ⁻¹⁰	5x10 ⁻¹⁰	5x10 ⁻¹⁰	5x10 ⁻¹⁰	5x10 ⁻¹⁰	5x10 ⁻¹⁰
C_{fe}	5.2i	5.2i	5.2i	5.2i	5.2i	5.2i	5.2i
C_{me}	2.0i	2.0i	2.0i	2.0i	2.0i	2.0i	2.0i
C_D	1.3i	1.3	1.3i	1.3i	1.3i	1.3i	1.3i
$C_T : F = 1$	0.1	0.2	0.2	0.2	0.5	0.5	0.7
$F = 0.6$	0.2	0.4	0.4	0.6	0.7	0.7	1.0
$F = 0.1$	0.6	0.8	0.8	1.0	0.9	0.9	1.2
C_S	0.8i	0.8i	0.8i	0.8i	0.8i	0.8i	0.8i
C_{mh}	0.8i	0.8i	0.8i	0.8i	0.8i	0.8i	0.8i
C_{fh}	5.2i	5.2i	5.2i	5.2i	5.2i	5.2i	5.2i

Figures 11 (a) to (d) show a comparison of model calculations (dashed lines) with experimental traces at T=80K obtained at different Δ_M and pulse fluences as labeled. For $\Delta_M = 10\text{meV}$ (Fig. 11 (a)) the excitation density was divided into $n_{exc,f} = 0.4 \times 10^{16} \text{ cm}^{-3}$ and $n_{exc,m} = 1.6 \times 10^{16} \text{ cm}^{-3}$ at maximum pulse fluence $F = 1$.

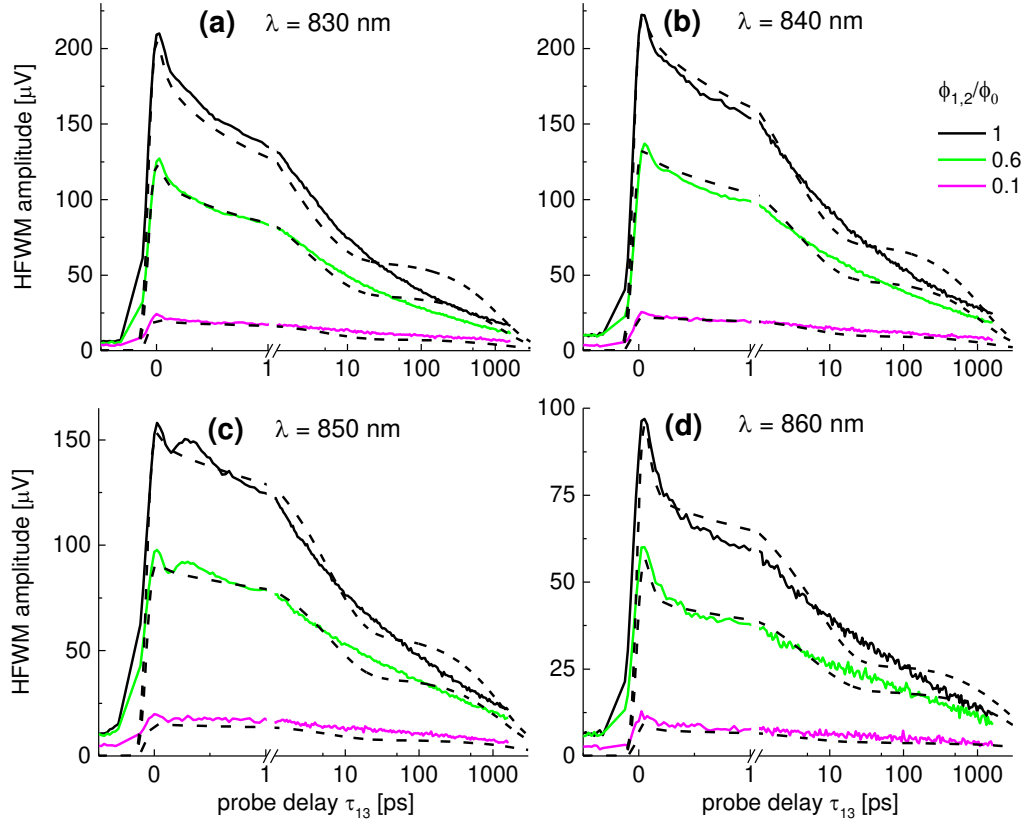


Figure 11: Comparison of calculated HFWM traces (dashed black lines) obtained from eqs. (3) and (4) with experimental data (full lines) acquired at excitation wavelengths (a) $\lambda_{\text{exc}} = 830\text{nm}$, (b) 840nm , (c) 850nm and (d) 860nm at various excitation fluences $\phi_{1,2}/\phi_0$ as labeled.

To estimate the excitation of donor bound transition a band was introduced to the absorption model described in chapter C with a FWHM of 21meV at 1.481eV using an excitation density of $n_{\text{exc,D}} = 0.4 \times 10^{16}\text{cm}^{-3}$ at $F = 1$. For the excitation density of WZ/ZB e-h pairs a value of

$n_{\text{exc,T}} = 0.15 \times 10^{16}\text{cm}^{-3}$ was used, determined from the ODOS (see Fig. 6) integrated up to

15meV below the gap energy. The resulting HFWM amplitude using $C_{fe} = 5.2i$, $C_{me} = 2.0i$,

$C_D = 1.3i$, $C_S = 0.8i$, $C_{mh} = 0.8i$, $C_{fh} = 5.2i$ and $C_T = 0.1$ is shown in Fig. 11 (a) as dashed line,, for pulse ratios $\phi_{1,2}/\phi_0 = 1, 0.6$ and 0.1 . In these calculations all parameters described above as well as the proportionality factor B were kept the same with the exception of C_T which was increased from 0.1 to 0.2 and 0.5, respectively, to achieve agreement with the experimental data. A summary of the parameters used in the simulations is given in table 1. For $\Delta_M = -7\text{meV}$ (see Fig. 11 (b)) we used $n_{exc,f} = 0.1 \times 10^{16} \text{ cm}^{-3}$, $n_{exc,m} = 1.2 \times 10^{16} \text{ cm}^{-3}$, $n_{exc,D} = 0.37 \times 10^{16} \text{ cm}^{-3}$ according to the spectral overlap of the excitation pulse. The excitation density of $n_{exc,T} = 0.15 \times 10^{16} \text{ cm}^{-3}$ was kept constant. The C parameters were kept the same as $\Delta_M = 10\text{meV}$ except for C_T which was changed to 0.2, 0.4 and 0.8 for $F = 1, 0.6, 0.1$, respectively. The dashed lines in Fig. 10 (b) show the resulting HFWM amplitude curves for different pump pulse fluences as labeled. For $\Delta_M = -20\text{meV}$ (see Fig. 11 (c)) we used $n_{exc,f} = 0$, $n_{exc,m} = 0.2 \times 10^{16} \text{ cm}^{-3}$, $n_{exc,D} = 0.08 \times 10^{16} \text{ cm}^{-3}$ and $n_{exc,T} = 0.15 \times 10^{16} \text{ cm}^{-3}$ according to the spectral overlap of the excitation pulse. The C parameters were kept the same as $\Delta_M = -7\text{meV}$. For $\Delta_M = -42\text{meV}$ (see Fig. 11 (d)) we used $n_{exc,f}$, $n_{exc,m}$ and $n_{exc,D}$ equal to zero and $n_{exc,T} = 0.06 \times 10^{16} \text{ cm}^{-3}$ according to the reduced overlap of the excitation pulse with the ODOS tail. The C parameters were kept the same as $\Delta_M = -20\text{meV}$ except $C_T = 0.2, 0.6$ and 1.0 was used for $F = 1, 0.6, 0.1$, respectively.

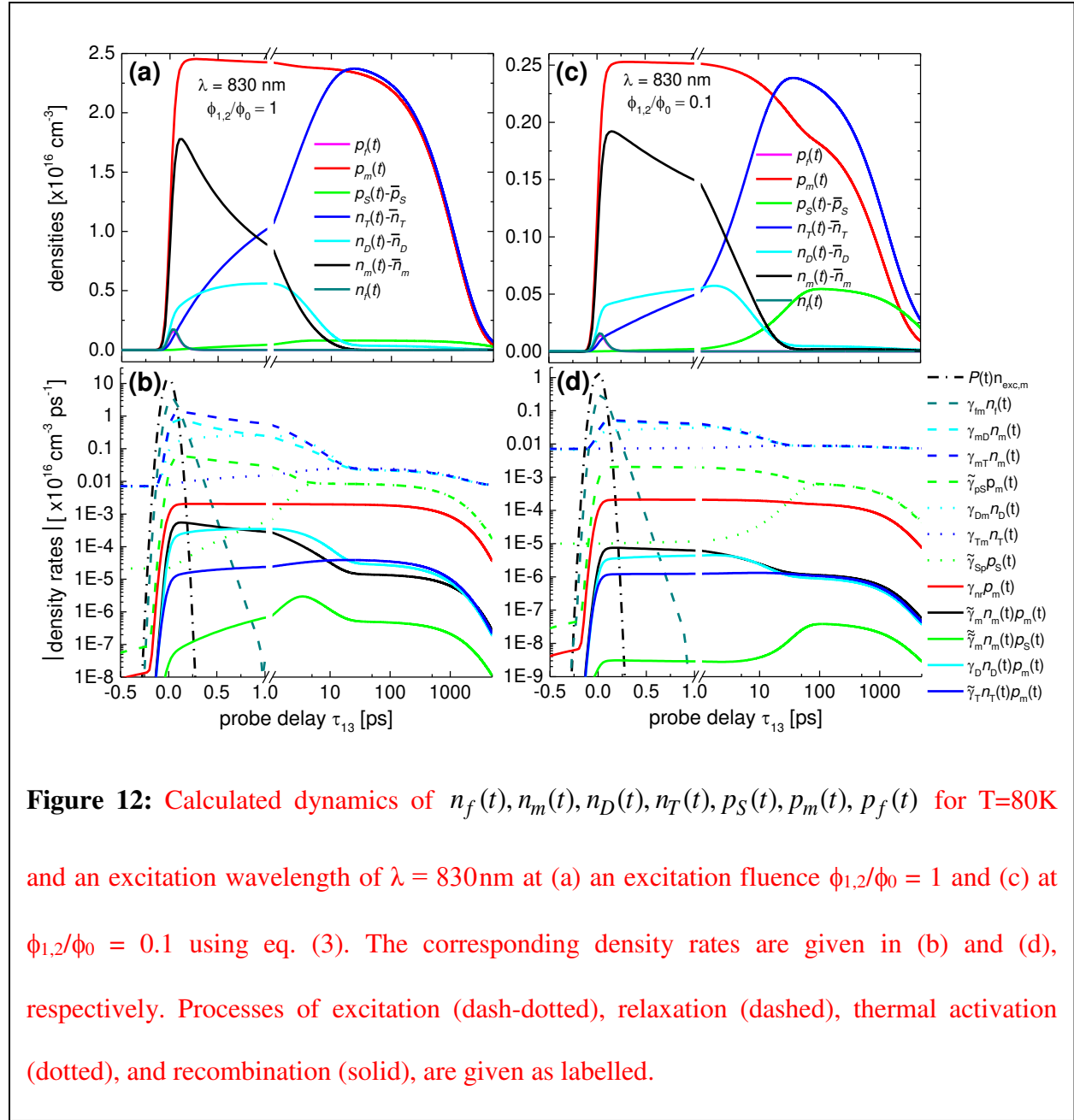
We find a general agreement of the calculated HFWM curves with the experimental data. Remaining deviations in the dynamics at delays above 30ps are attributed to the consideration of only one type of trapped ZB electrons described by the average localization energy $\Delta_T = 25\text{meV}$.

A more realistic consideration of a distribution of trapping sites with varying trapping energies and transition rates creating a distribution of decay times would likely remedy these deviations. However, the concurrent increase in the number of fit parameters would reduce the clarity of the results.

The coupled rate equations (3) allow analyzing the dynamics of densities $n_f, n_m, n_D, n_T, p_S, p_m, p_f$. Figure 12 (a,b) and (c,d) show an example of the calculated differences of carrier densities from their equilibrium values and the density rates for $\Delta_M=10\text{meV}$ at maximum pulse fluence $\phi_{1,2}/\phi_0 = 1$ and at lowest fluence $\phi_{1,2}/\phi_0 = 0.1$, respectively

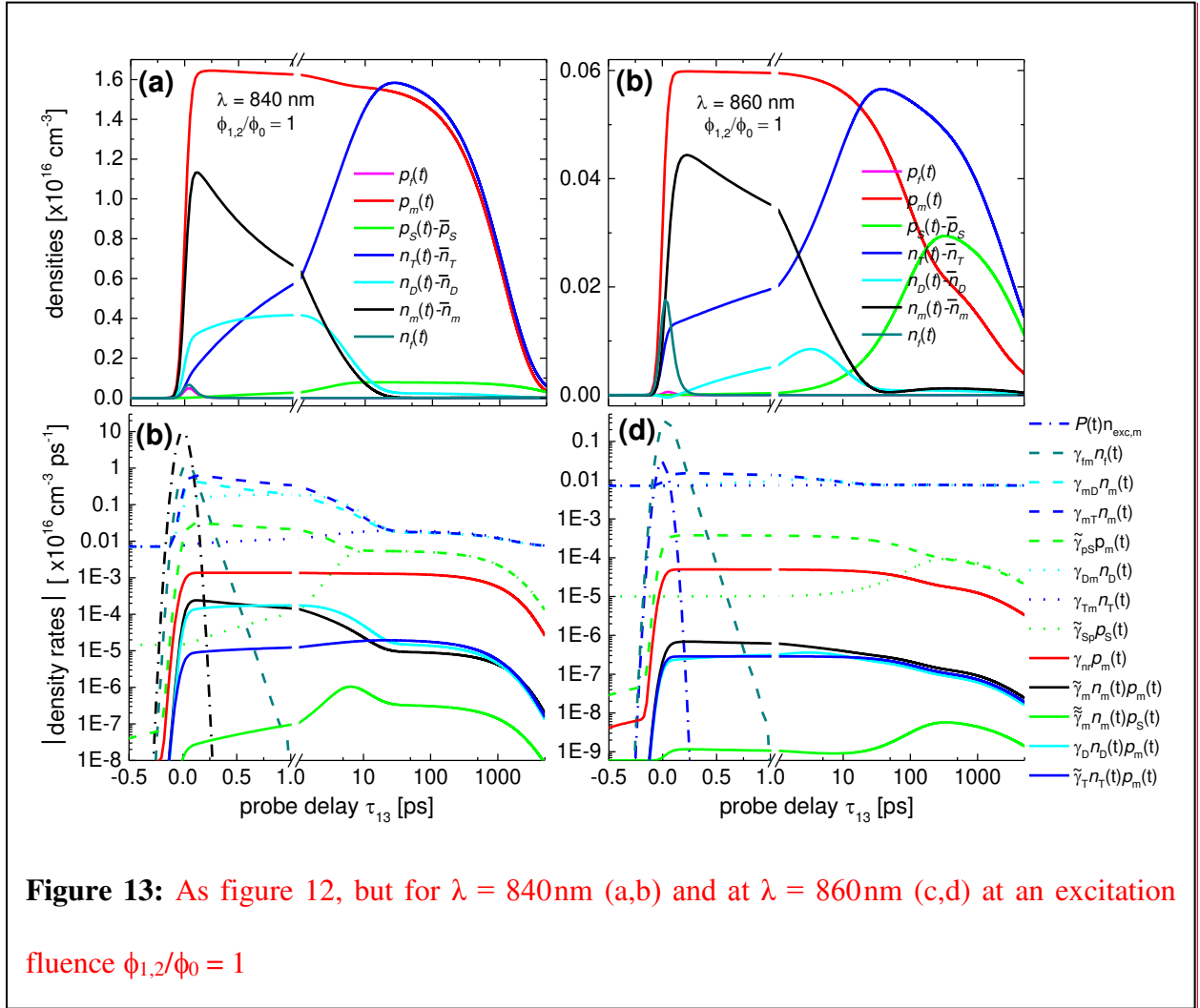
We discuss the results starting with $\phi_{1,2}/\phi_0 = 1$. The relaxation of the free electrons and holes is so fast that they relax within the excitation pulse duration to the mobility edge, and no significant free density builds up. The electrons at the mobility edge n_m , relax within the first picoseconds into the donor n_D and trapped ZB states n_T . This decay corresponds to T_1 of 0.7 ps of the multi-exponential fit (see eq. (2)) to the population dynamics shown in Fig. 5. The corresponding rates $\tilde{\gamma}_{mD}n_m$ and $\gamma_{mT}n_m$ are shown in Fig. 12 (b) as dashed cyan and blue lines. After about 1ps, n_m is sufficiently depleted so that the n_D thermally activate into n_m and then relax into n_T . Thermal equilibrium in the conduction band, between n_m , n_T , and n_D , is reached after about 10 ps as can be seen by the merging rates $\tilde{\gamma}_{mD}n_m$ and $\tilde{\gamma}_{Dm}n_D$, and of $\gamma_{mT}n_m$ and $\gamma_{Tm}n_T$, creating detailed balance. At about 5ps, the surface trapped holes come into thermal equilibrium with the mobile holes, as can be seen by the merging of the trapping rate $\tilde{\gamma}_{pS}p_m$ and thermal activation rate $\tilde{\gamma}_{Sp}p_S$. The surface hole density p_S is close to the saturation density p_{S0} . After intraband thermal equilibrium is established, the dynamics is dominated by the recombination of mobile holes. The non-radiative recombination is dominating (solid red line),

as dictated by the low quantum yield of about 2% at this temperature. The radiative recombination is dominated by the electrons in the ZB sections and the donor states, consistent with the observed PL spectrum (see Fig.2). The decay reduces the trapped hole density, which reduces the screening, and consequently decreases the thermally excited mobile hole density exponentially. This dramatically reduces the recombination for times above a nanosecond.



Turning now to the results for $\phi_{1,2}/\phi_0 = 0.1$ shown in Fig. 12 (c,d), the initial dynamics up to about 5ps shows a reduced decay rate due to the reduced carrier-carrier scattering. Importantly, since the photoexcited hole density p_m is smaller than the saturation density of surface holes p_{S_0} , the thermal activation is slower due to the larger activation energy, leading to a hole thermalization only after about 50ps. The subsequent population dynamics on the nanosecond time scale is again governed by the non-radiative recombination between mobile electrons and holes, fed by thermal activation of trapped electrons n_T and holes p_S . It is slower due to the reduced screening of the surface trapping potential.

[WL7] For excitation below the mobility edge, at $\Delta_M = -7, -20$, and -42meV , the population essentially remains the same but the decay rates are reduced due to the reduced inter-band excitation density. Fig. 13 (a) and (c) show as example the dynamics of densities at fluences $\phi_{1,2}/\phi_0 = 1$ for $\Delta_M = -7$ and -42meV , respectively, revealing decreasing initial decay rates of n_m and p_m . The reduced screening of the surface trapping potential leads to an increased hole thermalization time of 100ps for $\Delta_M = -42\text{meV}$ and provides a slower recombination dynamics.



The temperature dependence of the modeled dynamics is shown in Figures 14 (a) – (c) giving the calculated HFWM amplitude and the experimental data obtained at 150K, 210K and 270K.

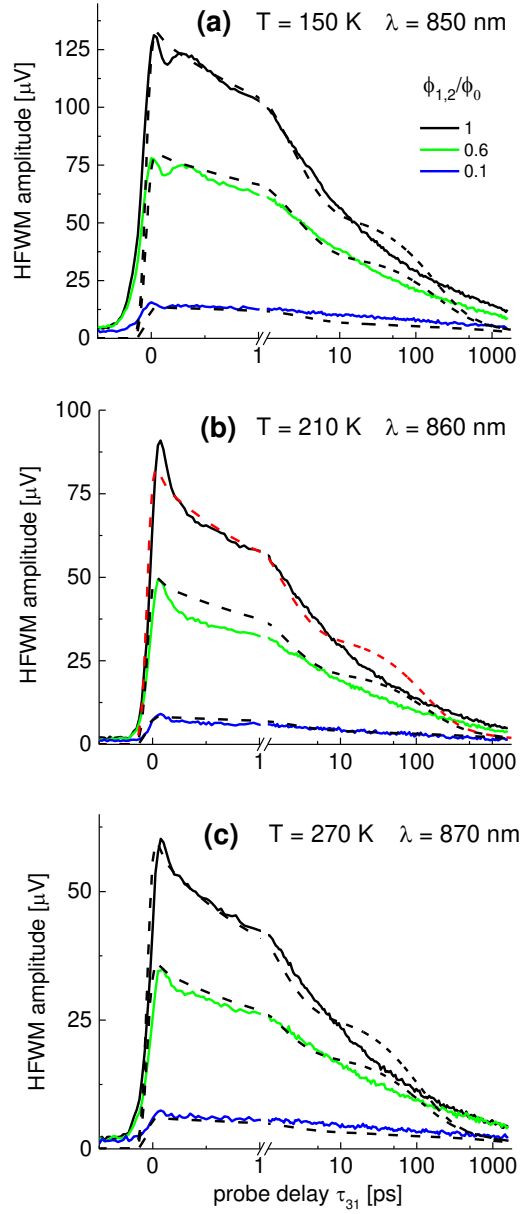


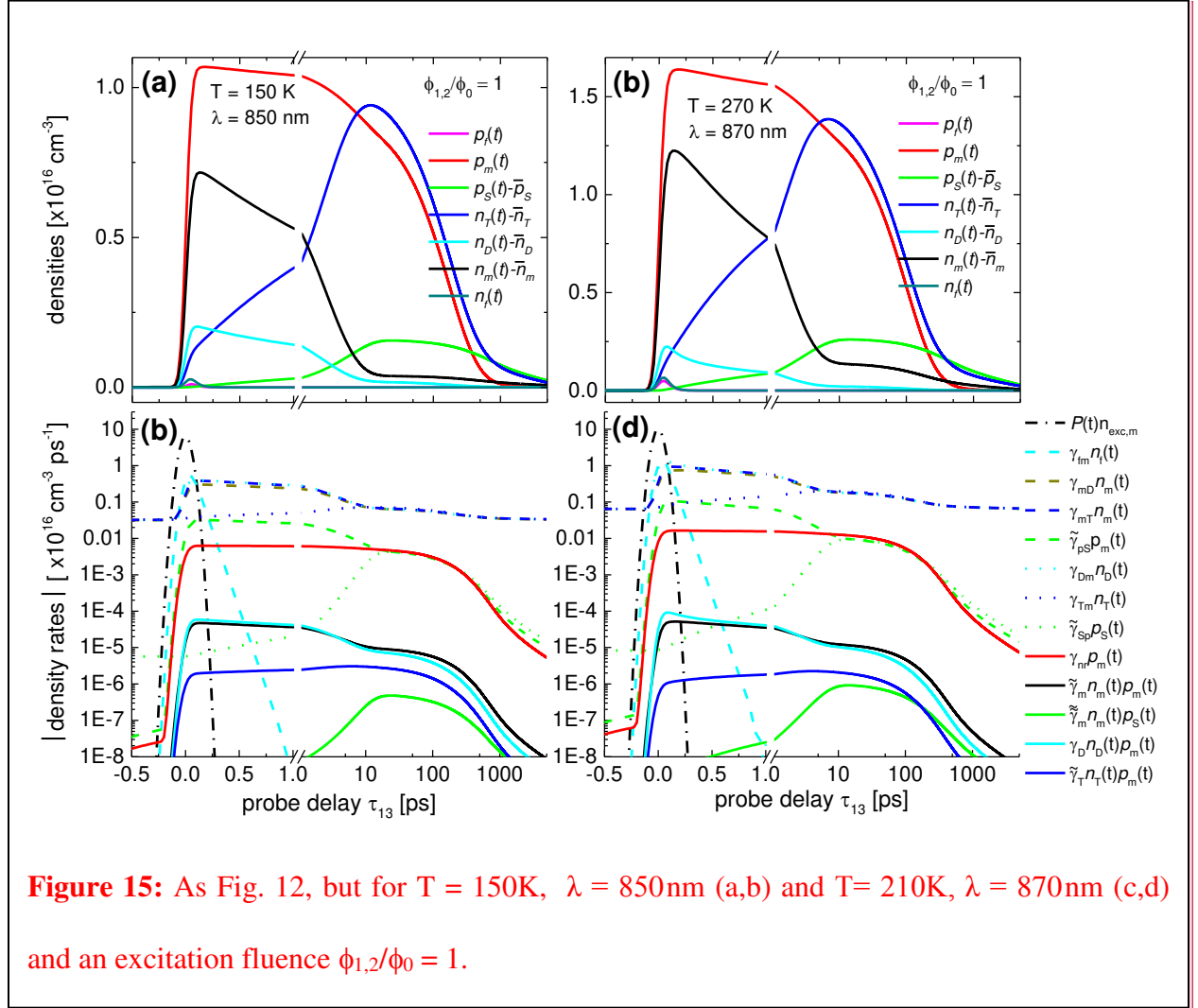
Figure 14: Comparison of calculated HFWM (dashed black lines) obtained from eqs. (3) and (4) with experimental data (full lines) at temperatures (a) $T = 150\text{K}$, (b) 210K , (c) 270K and various excitation fluences $\phi_{1,2}/\phi_0$ as labeled.

[WL9] Besides using the determined non-radiative rates γ_{nr} , as a function of temperature (see Fig.

all other relaxation and bimolecular rate constants were kept equal to the $T = 80\text{K}$ calculations. For $T = 150\text{K}$ we used $n_{exc,f} = 0$, $n_{exc,m} = 0.7 \times 10^{16} \text{ cm}^{-3}$, $n_{exc,D} = 0.26 \times 10^{16} \text{ cm}^{-3}$ and $n_{exc,T} = 0.15 \times 10^{16} \text{ cm}^{-3}$ according to the pulse overlap with the exciton and donor transition bands. In addition parameter C_T was adjusted to 0.5. At 210K and 270K we have $\Delta_M \sim -10\text{meV}$, so that we used the same excitation densities and imaginary C parameters were used as for $\Delta_M \sim -7\text{meV}$ at $T = 80\text{K}$. The C_T values were adjusted to 0.5 at $T = 210\text{K}$ and to 0.7 at $T = 270\text{K}$. (A summary of the used parameters is shown in table 1). As mentioned earlier the consideration of a distribution of ZB electrons with varying trapping energies and transition rates would likely lead to a better agreement between the calculation and the experimental data. The calculations also reproduce the data at lower pump pulse fluences (see Figs. 11 (a) – (c) for $F = 0.6$ and 0.1) using the same parameters as for $F = 1$ but increasing C_T values as shown in table 1.

The resulting densities $n_f, n_m, n_D, n_T, p_S, p_m, p_f$ at different temperatures are shown in Fig. 15 (a) and (c) for a fluence of $\phi_{1,2}/\phi_0 = 1$ for 150K and 270 K and the corresponding rates are given in Fig. 15 (b) and (d). The main temperature dependence is a shortening of the thermalization times due to the faster thermally activated rates, yielding about 10ps for electrons and holes at 150K, and 5ps at 300K. Due to the large trapping energy of the surface holes, which can be screened by the surface hole density, the longer dynamics remains remarkably independent on temperature, as there is an equilibrium density of surface holes established by the pulse repetition rate, which screens the trapping energy and thus modifies the thermally activated

population of mobile holes, to adjust the average decay rate to match the average excitation rate.



IV. CONCLUSIONS

We studied the dephasing and population dynamics of e-h pairs in polytype InP nanowires using three-beam HFWM, for excitation densities in the 10^{15} - 10^{16} cm^{-3} range and temperatures from 80K to 270K. The population dynamics shows processes with time constants spanning the full measured range of timescales, from 100fs to 100ns. With increasing excitation density the faster components in the sub-nanosecond range get more prominent. The dynamics has been interpreted by a coupled rate equation model which considers wurzite and zincblende electron

states, donor electron states, and band bending trapping holes to the surface. Intraband scattering rates respecting detailed balance are used, and screening of the band bending. Bimolecular recombination leads to interband relaxation, and is separated into radiative and non-radiative processes using non-radiative rates taken from the measured temperature dependent quantum yield. The model reproduces the essential features of the experimentally observed dynamics at different excitation wavelengths, pump-pulse fluences and lattice temperatures. Important conclusions are that intraband thermalization is reached within 5-50ps, after which the non-radiative recombination dominates the dynamics. Notably, the screenable surface band bending results in long lived spatially separated carriers, having a density which self-adjusts to balance the time-averaged excitation and recombination rates. In experiments with high repetition rates, often used in the literature, this provides a photogenerated, spatially separated background carrier density important for the measured dynamics. The model can be used and expanded in the future to interpret the carrier dynamics of similar structures. Using the amplitude and phase of the FWM data would result in a better separation of the difference processes, and an explicit fit of the model to the data could retrieve the free parameters in a more reliable fashion.

Photon echo experiments at $T = 80\text{K}$ reveal an exciton dephasing time of less than 100fs, while a time of several hundred fs is expected. We attribute this shorter than expected dephasing time to exciton-carrier scattering which is consistent with the typical donor concentration in these InP NWs in the order of $1 \times 10^{16} \text{ cm}^{-3}$ ⁶¹.

ACKNOWLEDGMENTS

The authors acknowledge Dr. G. Duscher, Dr. O. Dyck and Dr. M. Fickenscher for providing high resolution transmission electron microscope (HRTEM) images and fruitful discussion. The Australian Research Council (ARC) is acknowledged for its financial support and the authors

also acknowledge the use of facilities in the ACT node of the Australian National Fabrication Facility. Support from the Faculty Development Council (FDC) and the University Research Council (URC) at the University of Cincinnati is kindly acknowledged.

References

- [1] X. Zhou, S. A. Dayeh, D. Aplin, D. Wang, and E. T. Yu, Appl. Phys. Lett. **89**, 053113 (2006).
- [2] J. F. Wang, M. S. Gudiksen, X. F. Duan, Y. Cui, and C. M. Lieber, Science **293**, 1455 (2001).
- [3] T. B. Hoang, L. V. Titova, J. M. Yarrison-Rice, H. E. Jackson, A. O. Govorov, Y. Kim, H. J. Joyce, H. H. Tan, C. Jagadish, and L. M. Smith, Nano Lett. **7**, 588 (2007).
- [4] A. Mishra, L. V. Titova, T. B. Hoang, H. E. Jackson, L. M. Smith, J. M. Yarrison-Rice, Y. Kim, H. J. Joyce, Q. Gao, H. H. Tan, and C. Jagadish, Appl. Phys. Lett. **91**, 263104 (2007).
- [5] R. S. Wagner and W. C. Ellis, Appl. Phys. Lett. **4**, 89 (1964).
- [6] X. F. Duan and C. M. Lieber, Advanced Materials **12**, 298 (2000).
- [7] Q. Gao, H. H. Tan, H. E. Jackson, L. M. Smith, J. M. Yarrison-Rice, J. Zou, and C. Jagadish, Semiconductor Science and Technology **26**, 014035 (2011).
- [8] T. J. Trentler, K. M. Hickman, S. C. Goel, A. M. Viano, P. C. Gibbons, and W. E. Buhro, Science **270**, 1791 (1995).
- [9] D. S. Xu, D. P. Chen, Y. J. Xu, X. S. Shi, G. L. Guo, L. L. Gui, and Y. Q. Tang, Pure Appl. Chem. **72**, 127 (2000).
- [10] Q. Gao, D. Saxena, F. Wang, L. Fu, S. Mokkalapati, Y. Guo, L. Li, J. Wong-Leung, P. Caroff, H. H. Tan, and C. Jagadish, Nano Letters **14**, 5206 (2014).
- [11] K. Tomioka, T. Tanaka, S. Hara, K. Hiruma, and T. Fukui, IEEE Journal of Selected Topics in Quantum Electronics **17**, 1112 (2011).

- [12] M. Montazeri, M. Fickenscher, L. M. Smith, H. E. Jackson, J. Yarrison-Rice, J. H. Kang, Q. Gao, H. H. Tan, C. Jagadish, Y. N. Guo, J. Zou, M. E. Pistol, and C. E. Pryor, *Nano Letters* **10**, 880 (2010).
- [13] Y. Masumoto, K. Goto, S. Yoshida, Y. Sakuma, P. Mohan, J. Motohisa, and T. Fukui, *Phys. Rev. B* **82**, 075313 (2010).
- [14] S. Paiman, Q. Gao, H. H. Tan, C. Jagadish, K. Pemasiri, M. Montazeri, H. E. Jackson, L. M. Smith, J. M. Yarrison-Rice, X. Zhang, and J. Zou, *Nanotechnology* **20**, 225606 (2009).
- [15] M. E. Reimer, M. P. van Kouwen, M. Barkelid, M. Hocevar, M. H. M. van Weert, R. E. Algra, E. Bakkers, M. T. Bjork, H. Schmid, H. Riel, L. P. Kouwenhoven, and V. Zwiller, *J. Nanophotonics* **5**, 053502 (2011).
- [16] M. E. Reimer, M. P. van Kouwen, A. W. Hidma, M. H. M. van Weert, E. Bakkers, L. P. Kouwenhoven, and V. Zwiller, *Nano Lett.* **11**, 645 (2010).
- [17] M. H. M. van Weert, N. Akopian, U. Perinetti, M. P. van Kouwen, R. E. Algra, M. A. Verheijen, E. Bakkers, L. P. Kouwenhoven, and V. Zwiller, *Nano Lett.* **9**, 1989 (2009).
- [18] K. Pemasiri, M. Montazeri, R. Gass, L. M. Smith, H. E. Jackson, J. Yarrison-Rice, S. Paiman, Q. Gao, H. H. Tan, C. Jagadish, X. Zhang, and J. Zou, *Nano Lett.* **9**, 648 (2009).
- [19] A. Maharjan, K. Pemasiri, P. Kumar, A. Wade, L. M. Smith, H. E. Jackson, J. M. Yarrison-Rice, A. Kogan, S. Paiman, Q. Gao, H. H. Tan, and C. Jagadish, *Appl. Phys. Lett.* **94**, 193115 (2009).
- [20] N. Akopian, G. Patriarche, L. Liu, J. C. Harmand, and V. Zwiller, *Nano Lett.* **10**, 1198 (2010).

- [21] D. Spirkoska, J. Arbiol, A. Gustafsson, S. Conesa-Boj, F. Glas, I. Zardo, M. Heigoldt, M. H. Gass, A. L. Bleloch, S. Estrade, M. Kaniber, J. Rossler, F. Peiro, J. R. Morante, G. Abstreiter, L. Samuelson, and A. Fontcuberta i Morral, *Phys. Rev. B* **80**, 245325 (2009).
- [22] X. F. Duan, Y. Huang, R. Agarwal, and C. M. Lieber, *Nature* **421**, 241 (2003).
- [23] D. Saxena, S. Mokkapat, P. Parkinson, N. Jiang, Q. Gao, H. H. Tan, and C. Jagadish, *Nature Photonics* **7**, 963 (2013).
- [24] H.-G. Park, C. J. Barrelet, Y. Wu, B. Tian, F. Qian, and C. M. Lieber, *Nat. Photonics* **2**, 622 (2008).
- [25] A. Berg, S. Yazdi, A. Nowzari, K. Storm, V. Jain, N. Vainorius, L. Samuelson, J. B. Wagner, and M. T. Borgstrom, *Nano Lett.* **16**, 656 (2016).
- [26] Y. Zhang, J. Wu, M. Aagesen, and H. Liu, *J. Phys. D: Appl. Phys.* **48**, 463001 (2015).
- [27] H. T. Ng, J. Han, T. Yamada, P. Nguyen, Y. P. Chen, and M. Meyyappan, *Nano Lett.* **4**, 1247 (2004).
- [28] M. H. M. van Weert, M. den Heijer, M. P. van Kouwen, R. E. Algra, E. Bakkers, L. P. Kouwenhoven, and V. Zwiller, *Appl. Phys. Lett.* **96**, 233112 (2010).
- [29] M. P. van Kouwen, M. E. Reimer, A. W. Hidma, M. H. M. van Weert, R. E. Algra, E. Bakkers, L. P. Kouwenhoven, and V. Zwiller, *Nano Lett.* **10**, 1817 (2010).
- [30] J. Heinrich, A. Huggenberger, T. Heindel, S. Reitzenstein, S. Hofling, L. Worschech, and A. Forchel, *Appl. Phys. Lett.* **96**, 211117 (2010).
- [31] M. N. Makhonin, A. P. Foster, A. B. Krysa, P. W. Fry, D. G. Davies, T. Grange, T. Walther, M. S. Skolnick, and L. R. Wilsont, *Nano Lett.* **13**, 861 (2013).

- [32] M. P. van Kouwen, M. H. M. van Weert, M. E. Reimer, N. Akopian, U. Perinetti, R. E. Algra, E. Bakkers, L. P. Kouwenhoven, and V. Zwiller, *Appl. Phys. Lett.* **97**, 113108 (2010).
- [33] A. Othonos, E. Lioudakis, D. Tsokkou, U. Philipose, and H. E. Ruda, *Journal of Alloys and Compounds* **483**, 600 (2009).
- [34] H. J. Joyce, P. Parkinson, N. Jiang, C. J. Docherty, Q. Gao, H. H. Tan, C. Jagadish, L. M. Herz, and M. B. Johnston, *Nano Lett.* **14**, 5989 (2014).
- [35] L. V. Titova, T. B. Hoang, J. M. Yarrison-Rice, H. E. Jackson, Y. Kim, H. J. Joyce, Q. Gao, H. H. Tan, C. Jagadish, X. Zhang, J. Zou, and L. M. Smith, *Nano Letters* **7**, 3383 (2007).
- [36] T. T. T. Vu, T. Zehender, M. A. Verheijen, S. R. Plissard, G. W. G. Immink, J. E. M. Haverkort, and E. P. A. M. Bakkers, *Nanotechnology* **24**, 115705 (2013).
- [37] S. Crankshaw, S. Reitzenstein, L. C. Chuang, M. Moewe, S. Muench, C. Boeckler, A. Forchel, and C. Chang-Hasnain, *Phys. Rev. B* **77**, 235409 (2008).
- [38] C. K. Yong, J. Wong-Leung, H. J. Joyce, J. Lloyd-Hughes, Q. Gao, H. H. Tan, C. Jagadish, M. B. Johnston, and L. M. Herz, *Nano Letters* **13**, 4280 (2013).
- [39] D. S. Chemla and J. Shah, *Nature* **411**, 549 (2001).
- [40] W. Langbein, H. Gislason, and J. M. Hvam, *Phys. Rev. B* **60**, 16667 (1999).
- [41] E. J. Mayer, J. O. White, G. O. Smith, H. Lage, D. Heitmann, K. Ploog, and J. Kuhl, *Phys. Rev. B* **49**, 2993 (1994).
- [42] T. Baars, W. Braun, M. Bayer, and A. Forchel, *Phys. Rev. B* **58**, R1750 (1998).
- [43] W. Braun, M. Bayer, A. Forchel, H. Zull, J. P. Reithmaier, A. I. Filin, and T. L. Reinecke, *Phys. Rev. B* **56**, 12096 (1997).

- [44] H. P. Wagner, H. P. Tranitz, W. Langbein, J. M. Hvam, G. Bacher, and A. Forchel, *Physica Status Solidi B* **231**, 11 (2002).
- [45] H. P. Wagner, W. Langbein, J. M. Hvam, G. Bacher, T. Kummell, and A. Forchel, *Phys. Rev. B* **57**, 1797 (1998).
- [46] H. P. Wagner, H. P. Tranitz, R. Schuster, G. Bacher, and A. Forchel, *Phys. Rev. B* **63**, 155311/1 (2001).
- [47] W. Langbein, *Rivista Del Nuovo Cimento* **33**, 255 (2010).
- [48] W. Langbein and B. Patton, *Journal of Physics-Condensed Matter* **19**, 295203 (2007).
- [49] M. Kaveh, G. Duscher, Q. Gao, C. Jagadish, and H. P. Wagner, *Mater. Res. Express* **2**, 045001 (2015).
- [50] A. Naeem, F. Masia, S. Christodoulou, I. Moreels, P. Borri, and W. Langbein, *Phys. Rev. B* **91**, 121302 (2015).
- [51] Y. T. Shih, W. C. Chiang, C. S. Yang, M. C. Kuo, and W. C. Chou, *J. Appl. Phys* **92**, 2446 (2002).
- [52] E. G. Gadret, M. M. de Lima, Jr., J. R. Madureira, T. Chiaramonte, M. A. Cotta, F. Iikawa, and A. Cantarero, *Appl. Phys. Lett.* **102**, 122101 (2013).
- [53] S. Rudin, T. L. Reinecke, and B. Segall, *Phys. Rev. B* **42**, 11218 (1990).
- [54] L. Zhang, J.-W. Luo, A. Zunger, N. Akopian, V. Zwiller, and J.-C. Harmand, *Nano Lett.* **10**, 4055 (2010).
- [55] M. Murayama and T. Nakayama, *Phys. Rev. B* **49**, 4710 (1994).
- [56] M. Gurioli, A. Vinattieri, J. Martinezpascor, and M. Colloci, *Phys. Rev. B* **50**, 11817 (1994).

- [57] W. Langbein, S. Hallstein, H. Kalt, R. Notzel, and K. Ploog, Phys. Rev. B **51**, 1946 (1995).
- [58] W. J. Turner, W. E. Reese, and G. D. Pettit, Phys. Rev **134**, 1467 (1964).
- [59] M. De Luca, A. Zilli, H. A. Fonseca, S. Mokkaṭṭi, A. Miriametro, H. H. Tan, L. M. Smith, C. Jagadish, M. Capizzi, and A. Polimeni, Nano Lett. **15**, 998 (2015).
- [60] U. Strauss, W. W. Ruhle, and K. Kohler, Appl. Phys. Lett. **62**, 55 (1993).
- [61] H. J. Joyce, C. J. Docherty, Q. Gao, H. H. Tan, C. Jagadish, J. Lloyd-Hughes, L. M. Herz, and M. B. Johnston, Nanotechnology **24**, 214006 (2013).
- [62] D. S. Kim, J. Shah, J. E. Cunningham, T. C. Damen, W. Schafer, M. Hartmann, and S. Schmittrink, Physical Review Letters **68**, 1006 (1992).
- [63] L. Schultheis, J. Kuhl, A. Honold, and C. W. Tu, Physical Review Letters **57**, 1635 (1986).
- [64] L. C. Andreani, A. Dandrea, and R. Delsole, Physics Letters A **168**, 451 (1992).
- [65] M. S. Skolnick and P. J. Dean, J. Phys. C: Solid State Phys. **15**, 5863 (1982).